OPTICAL AND THERMAL STUDIES OF DEEP LEVELS IN ANION DEFICIENT Al_2O_3:C

By

VON HOWARD WHITLEY

Bachelor of Science

University of Texas

Austin, Texas

1994

Submitted to the Faculty of the
Graduate College of the
Oklahoma State University
in partial fulfillment of
the requirements for
the Degree of
DOCTOR OF PHILOSOPHY
May, 2000

OPTICAL AND THERMAL STUDIES

OF DEEP LEVELS IN ANION

DEFICIENT Al_2O_3:C

Thesis Approved:

Thesis Advisor

Dean of the Graduate College

ACKNOWLEDGMENTS

I would like to first show my gratitude and appreciation to my wife Lori who always offered support and encouragement when I needed it most.

I would like to thank my advisor, Dr. Stephen McKeever, who did an excellent job of advising and steering me. He taught me the difference between quality science and junk. He has a great ability in the ways of science, teaching, and organization which I believe are unmatched. I only hope that I can live up the precidence that he has set before me.

I would like to thank Dr. Niels Agersnap Larsen who provided many stimulating conversations at odd hours of the morning.

I would like to thank my family, who thought this idea of Physics was completely insane, but nonetheless supported me.

I would like to thank all of my friends who have served as a healthy diversion from physics. I do not believe I could have finished without others around to take my mind off of my work.

Lastly, I would like to thank the office staff which keep the hum of the physics department up and running. I would like to extend a special thanks to Susan Cantrell who has solved so many problems and saved me so much time. Without her help, it would have taken much longer to complete my thesis.

TABLE OF CONTENTS

Chapter Page

LIST OF FIGURES

Figure Page

Chapter 1
INTRODUCTION

Aluminum Oxide, alumina, and corundum are some of the more frequent names that describe the crystalline form of $\alpha - Al_2O_3$. It has many uses currently in the modern world. Alumina is well known for its hardness and durability. It has long occupied an elevated place on the Mohs' hardness test [1], being one of the hardest naturally occuring substances known, second only to diamond. This hardness and durability has resulted in its use as an abrasive for sandpaper, cutting tools, polishing agents, body armor, dental implants and joint replacements. Alumina is also well known as one of the best electrical insultors.[2] It is often used as an insulator in spark plugs, high voltage power lines, components for electron tubes, and the like. [3] But for our current purposes in this work, the most important of its uses is its relatively recent application as a radiation dosimeter.

1.1 History of Al_2O_3 in Dosimetry

Corundum, emery, sapphire and ruby are forms found in nature having uses as abrasives and gemstones, dating from antiquity. Its use as a radiation dosimeter, however, dates from more recent times. The spark that started alumina down the road to its present place as a personal dosimeter can probably be traced to 1664 when Robert Boyle took a diamond to bed with him and noticed it glowed when held to his body.[5] According to McKeever[4],

this is one of the first known references to thermoluminescence in literature (although it was not called thermoluminescence at the time), and thermoluminescence is one of the key properties of alumina which has led to its recent popularity in dosimetry. If you had asked Sir Boyle to take alumina to bed with him as well, he would have had no idea what it was. According to Gitzen,[6] it was not until 1786 that de Morveau used the name "alumine" as the proper name for the basic earth of alum. The term was later anglicized to "alumina" in England, which is a term most often used interchangeably with the molecular formula, Al_2O_3.

More than one phase of Al_2O_3 exists, which generated considerable confusion for a time because different researchers used different nomenclatures for the various phases then known. The first known designations of α-Al_2O_3 and β-Al_2O_3 were assigned by Rankin and Merwin[7] in 1916. Ulrich [8] and Haber[9] added the γ phase in 1925. Frary[10] revised the nomenclature in 1946 by initially assigning greek letters to the phases by relative abundances found in nature, which persists today for the nomenclature of the first few phases of alumina. Some twenty-one or so additional phases have been discovered in addition to these, consuming a large range of the greek alphabet in the process.[6] The single crystalline form used for the measurements in these papers falls into the α category. The rest of the phases will not be discussed.

Connecting irradiation of a material and the luminescence emitted from material during subsequent heating was rather illusive to early authors. According to McKeever[4], early interpretations of thermoluminescence ranged from heat being directly converted to light (Oldenburg in 1676) to 'a sulphur' which actually burned upon heating (Du Fay in

1726). By Becker's accord[11], the first careful investigation into radiation-induced luminescence, in this case thermoluminescence, was undertaken by Wiedemann & Schmidt in 1895, who used a variety of synthetically produced phosphors irradiated with an electron beam.

In the 1950's, work was undertaken to find materials for specific thermoluminescent applications. Unfortunately, the mechanisms responsible for thermoluminescence were unknown. Daniels and his collegues undertook a series of investigations on a variety of materials to try to better understand what causes the radiation induced thermoluminescence. These investigations eventually led to the first attempt to use alumina as a thermoluminescent material in 1958 by Rieke and Daniels[12]. Several different phases of Al_2O_3 were tried and up to four thermoluminescent peaks were found between 0-300 °C. Unfortunately, the radiation sensitivity of alumina at the time was considerably lower than other materials such as lithium fluoride (LiF), and consequently, its use as a dosimeter quickly died away.

The 1970's saw a resurgence in studies on alumina as a radiation dosimeter. The most important of the work was the identification of the emission centers in Al_2O_3. Seminal works by Evans and Staplebroek [13], Lee and Crawford[14], and Summers and collegues[15]- [18] finally led to a good understand of the processes responsible for the radiation induced luminescence and are argueably still the most important works on radiation induced emission in Al_2O_3 today. Although these important works were undertaken, the use of alumina as a dosimeter was still unpopular because the sensitivity of the material was still low in comparison to others.

In the 1990's, in search of a material that had a very low exo-electron emission, Al_2O_3:C was synthesized by Akselrod and collegues.[19] Much to their surprise, the material had a huge exo-electron emission.[20] Subsequent thermoluminescence measurements showed the material to be more than 50 times more sensitive than LiF. With the sensitivity problem overcome, the tide began to turn for Al_2O_3:C. In the mid 1990's, McKeever and collegues[21],[22] introduced an optical method used to stimulate the radiation-induced luminescence from the material. This method was even more sensitive than thermoluminescence and was subsequently patented. In the late 1990's, Landauer inc., licensed the technology from Oklahoma State University for use in its personal dosimetry business. Currently, Landauer inc., processes over one million Al_2O_3:C equipped badges per month, with Oklahoma State University being one of its customers.

1.2 Purpose

Even though the material is being currently used as a dosimeter, the trapping states are not well known. The mechanisms by which charge particles are excited from the trapping centers is only guessed to be both optical and thermal in nature. This body of work is undertaken in order to provide a better understanding of the relationship of these trapping centers with light and heat.

1.3 Al_2O_3: Crystalline structure and defects

The first approximate determination of the crystallographic structure of the α phase of Al_2O_3, dates back to the work of Bragg et al. [23] in 1915, and later by Pauling[24] in

1925. The structure of aluminum oxide consists of close packed planes of large oxygen ions forming a hexagonal close packed array. The aluminimum ions are placed on the octohedral sites of this basic array and form another type of distorted close packed plane which is inserted between the oxygen layers. To maintain charge neutrality, however, only two thirds of the octohedral sites available are filled with Al^{3+} ions. Figure 1.1 shows this structure, the large, dark gray spheres represent the O^{2-} ions and the smaller, light gray spheres represent the Al^{3+} ions. The center aluminum ion in this figure does not lay in the same plane as the other aluminum ions, but lies in the next aluminum plane above them. The aluminum site below this ion is empty to maintain charge neutrality. Figure 1.2 shows this same figure looking along the oxygen planes. Note that the aluminum ions between the O^{2-} planes do not all lie in the same plane, but actually lie in two separate planes between the oxygen planes. The shorter Al-O distance is 0.186 nm, while the longer Al-O bond is 0.197 nm. The overall symmetry is C_2.

The samples are grown from the melt at 2323 K in a highly reducing atmosphere in the presence of graphite (the so-called Stepanov process). The highly reducing atmosphere induces large concentrations of oxygen vacancies which play an integral part in the luminescence process.

The removal of an O^{2-} results in an oxygen vacancy center. Occupancy of this center by two electrons gives rise to a neutral F center, whereas occupancy by one electron forms a positively charged F^+ center (with respect to the lattice). In order to to have a large number of F^+ centers in as-grown specimens requires the presence of negatively charged

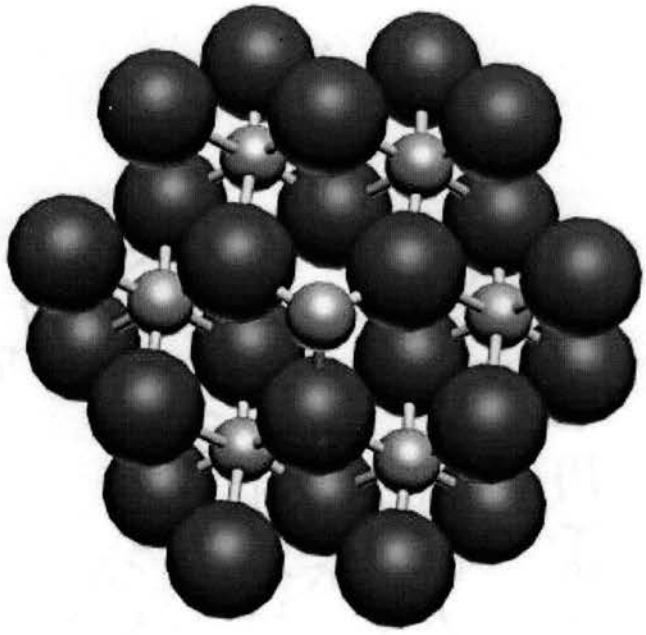

Figure 1.1 Crystalline structure of Al_2O_3 shown looking down on parallel oxygen planes. The oxygen ions are represented by the large spheres, the aluminum ions are represented by the small spheres.

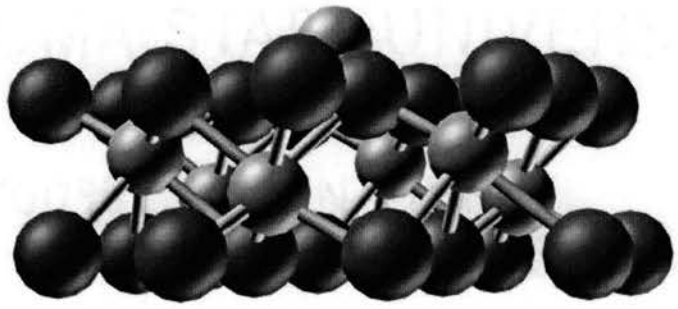

Figure 1.2 View of the structure down two parallel planes of O^{2-} ions. Notice in this view that the center Al^{3+} site is unoccupied. The center Al^{3+} shown in Fig.1.1 is actually lying in the next Al^{3+} plane above the O^{2-} ions. Also note that the two different Al-O bond lengths result in the Al^{3+} ions lying in two planes between the O^{2-} planes.

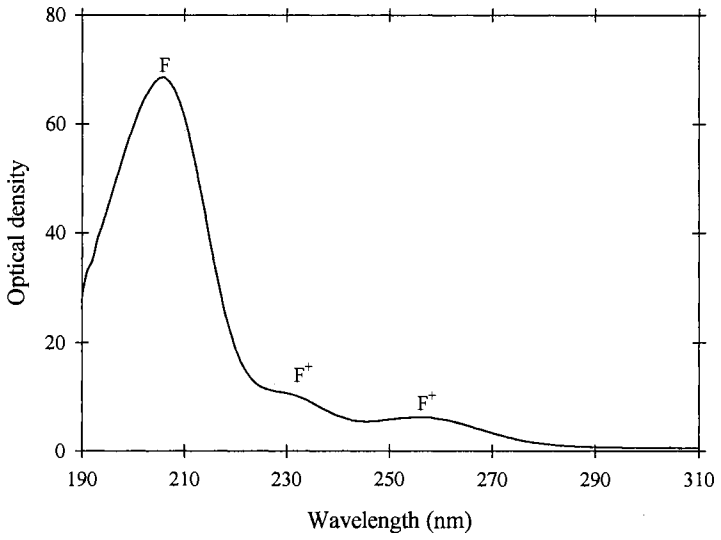

Figure 1.3 Optical absorption spectra of Al_2O_3:C over the range of 190-310 nm.

compensators. The presence of graphite allows for a C^{2+} impurity to substitute for Al^{3+} in order to provide charge compensation.[4]

A representative optical absorption of an unirradiated sample in fig.1.3 reveals the presence of F center absorption at 205nm (6.05eV) and F^+ absorption at 230 nm (5.4 eV) and 255 nm (4.8eV). An additional absorption band is thought to exist for the F^+ center around 6 eV.[13] However, the exact location is difficult to determine since the F center absorption overlaps it in this region. Using an oscillator strength of 1.3 for the F center and 0.66 for the F^+ center[14], the concentrations are found to be $(0.5\text{-}2.0)\text{x}10^{17}\text{cm}^{-3}$ and $(0.4\text{-}1.5)\text{x}10^{16}$ in TL-quality Al_2O_3:C.

Direct stimulation of the F center in the 205nm absorption band results in an emission at 420 nm with a lifetime of 35 ms at room temperature.[14],[16],[25] A schematic representation of the relaxation process is shown in Fig.1.4. Absorption of a 6.05 eV pho-

ton raises an electron from the ^{1}1A ground state to a ^{1}p-like excited state. This excited ^{1}p like state is believed to lie in the conduction band because photoconductivity is measured even at 10 K when stimulated at 6.05 eV.[17] According to Summers,[18] since there is only one F absorption band, the local symmetry is apparently not effective in splitting the p-like state possibly because it is very diffuse. The lifetime of the emission process is in the tens of milliseconds indicating that the transition is spin forbidden. This implies the emission state is a spin triplet and assumed to be ^{3}p-like.

The C_2 crystal field is expected to split the ^{3}p like state into three components with 1A, 1B and 2B character. The ^{1}p like state decays to the ^{3}p like state ^{3}1A, which is thought to be located ~1.6 eV below the relaxed ^{1}p-like state in the relaxed configuration. The decay from the ^{1}p-like state to the ^{3}1A state is non-radiative. The electron then decays from the ^{3}1A to the ^{3}2B and then the ^{3}1B. The electron can relax radiatively to the ground state from both the ^{1}1B and ^{3}2B states. Above 50 K, the splitting between the lowest states is small and only a single lifetime of 35 ms for the F center emission is seen. Below 50K, the lifetime of the F center is seen to have two components, one of which is attributed to decay from the ^{3}2B state, the other is attributed to decay from the ^{3}1B state.[16]

Stimulation into the 255, 230, or 205 nm absorption bands also produces F^+ center emission at 326 nm (3.8 eV) with a lifetime of $\leq$ 7ns. [13] A schematic representation of the F^+ center energy levels is shown in fig.1.5. These stimulation wavelengths produce 1A$\longrightarrow$1B (255 nm stimulation), 1A$\longrightarrow$2A (230 nm stimulation) and 1A$\longrightarrow$2B (>6 eV stimulation) transitions. Because the necessary absorption to produce a transition from 1A$\longrightarrow$2B overlaps with the F center absorption, the exact energy is unknown. An ad-

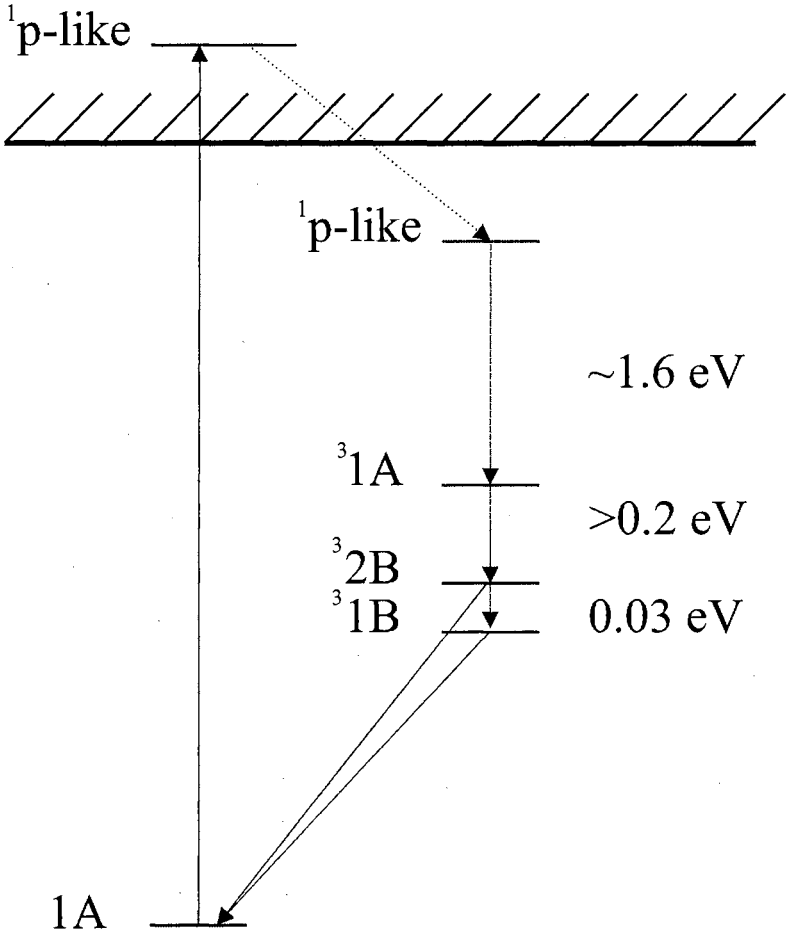

Figure 1.4 Schematic representation of the energy levels of the F Center in Al_2O_3 (adapted from Summers[18]).

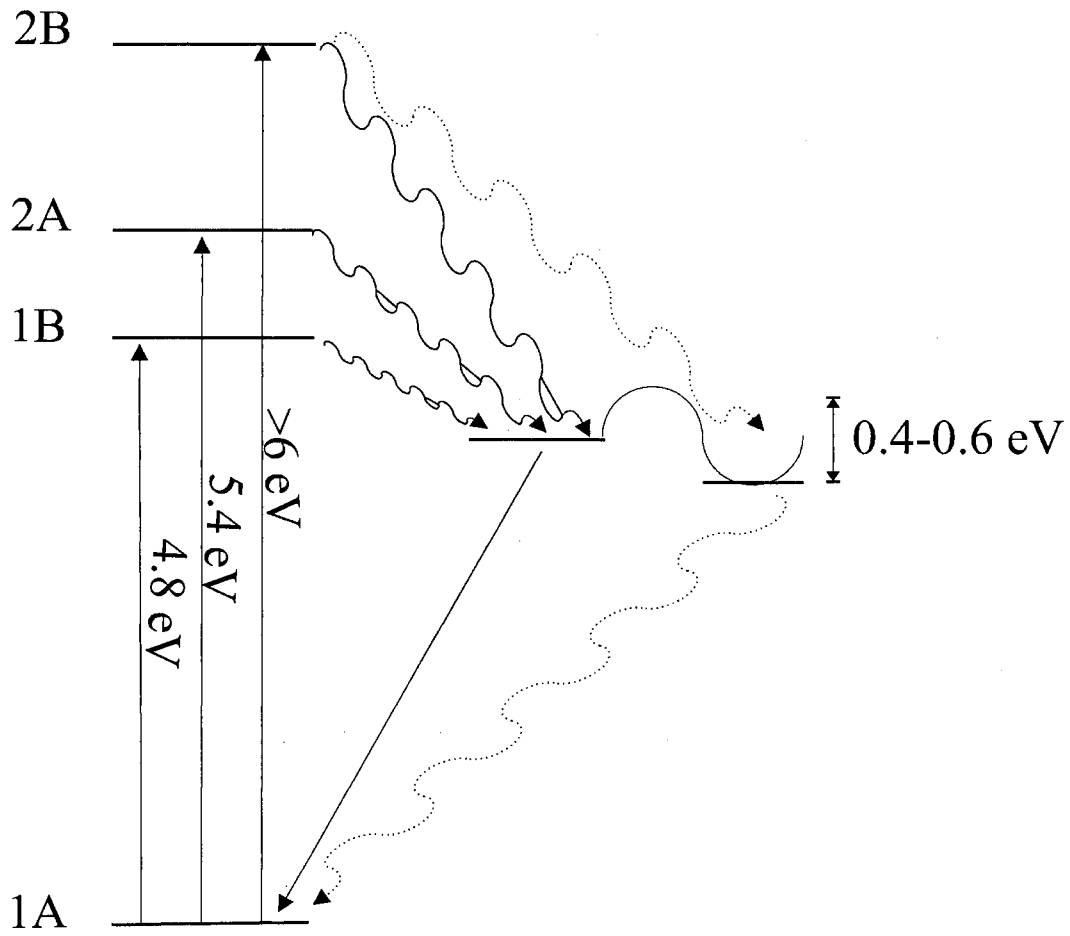

Figure 1.5 Schematic representation of the F^+ center energy levels. The straight lines represent optical absorption or emission. The wavy lines represent non optical relaxation.

ditional energy state is illustrated on the far right of Fig.1.5. Direct relaxation into this non-radiative center was suggested by Evans et al.[13] as a reason to explain the weak F^+ emission when stimulating into the 6 eV band. Thermal quenching measurements on the F^+ center in chapter 3 indicate that there is a non-radiative recombination center with a 0.6 eV energy barrier separating it and the radiative recombination center, which further supports the conclusion of Evans et al.

Chapter 2
LUMINESCENCE AND CONDUCTIVE PROCESSES IN Al_2O_3

Four different types of measurement were used in this work—thermoluminescence (TL), thermally stimulated conductivity (TSC), optically stimulated luminescence (OSL) and photoconductivity (PC). TL and TSC are both a result of thermal excitation of trapped charge carries and are closely related. OSL and PC result from optical excitation of trapped charge carriers and are also closely related. Figure 2.1 shows a band diagram overview of each. All of the information and conclusions in this thesis are a direct result of applications of these tools.

2.1 Thermal processes : Thermoluminescence

2.1.1 Introduction to TL

In the process of TL, a sample is first excited by irradiation at a 'low temperature'.[1] This irradiation is a means by which charge is freed from one location and trapped in other. The irradiation will either free charge from its ground state, which can then become trapped in charge traps, or the irradiation can cause already trapped charge to redistribute itself among the various trapping centers. Usually, the irradiations are performed using ionizining radiation (γ, α, β, x, etc.) or non ionizing radiation (UV to visible).

[1] The meaning of 'low temperature' will be discussed later

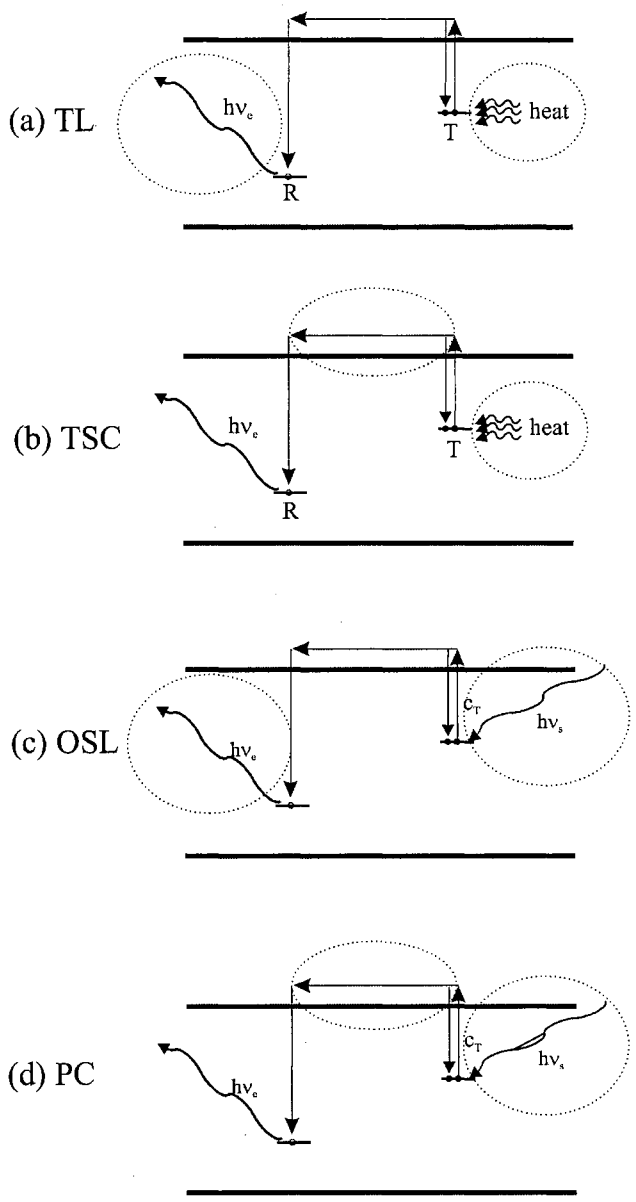

Figure 2.1 Schematic band diagram of the various processes discussed in Ch 2. The dotted circles highlight the relevant differences from the other experimental types.

In the case of ionizing radiation, the energy of the stimulation source is sufficient to ionize both electrons and holes across the band gap, allowing them to be trapped at various charge traps throughout the sample, thus populating the TL traps. In the case of non-ionizing radiation, the stimulation source does not have enough energy to ionize charge across the band gap. In alumina, it does have the energy to ionize F centers (provided that the energy of the stimulation light is $\gtrapprox$ 6.0 eV), liberating electrons which can fill electron traps. Non-ionizing radiation additionally can ionize charge carriers out of charge traps into the delocalized band. This redistribution of charge carriers is often referred to as photo-transferred thermoluminescence (PTTL) [32],[33].

Once the sample has been irradiated, the temperature of the sample is then raised linearly with time according to the function:

$$T_s[t] = T_0 + \beta t \tag{2.1}$$

where $T_s[t]$ is the temperature of the sample at a given time, T_0 is the starting temperature, β is the heating rate, and t is time.

The trapped charge carriers reside in a metastable state. At the 'low' irradiation temperature, the lifetime of the charges in the traps is very long. As the temperature of the sample is increased, the lifetime of the charge carrier in the trap decreases. Once the temperature of the sample is high enough, the trapped charge can be thermally excited into the delocailized band, at which point it can recombine with a recombination center, releasing light in the process. Thus the term 'low' temperature means any temperature in which the lifetime of the charge carriers in the traps is much longer than the time it takes to heat the sample to the maximum temperature.

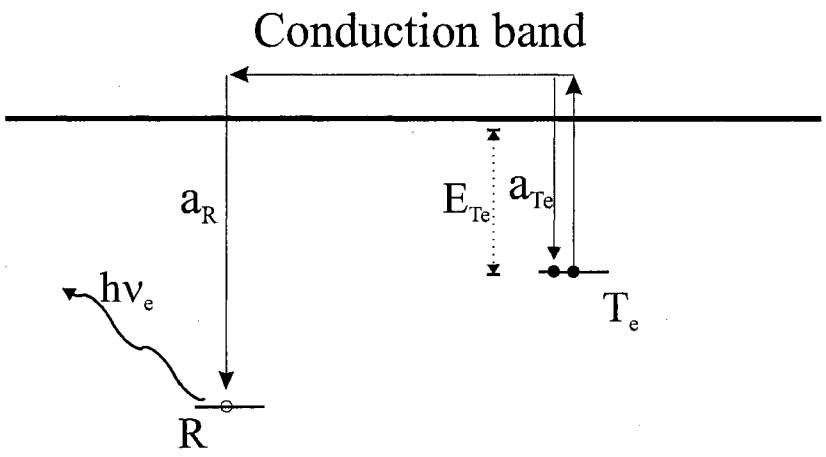

Figure 2.2 Band diagram showing the TL process. Electrons trapped at the trapping center T_e are thermally released and recombine with the recombination center R, releasing energy $h\nu_e$ in the form of light.

Figure 2.2 shows a model of the process consisting of one trap one recombination center R and one trapping center T_e with an activation energy of E_{T_e}.and a concentration of N. The population of electrons in trap T_e is n and in the conduction band is n_c. The concentration of charge in the recombination centers is m. At a temperature T, the trapped electrons are thermally released into the conduction band at a rate of $sn\exp\{-\frac{E_{T_e}}{kT}\}$ where s is the frequency factor, and k is Boltzmann's constant.

The kinematic rate equations describing the redistribution of electrons among the trapping center, conduction band and recombination center are:

$$\begin{aligned}
\frac{dn_c}{dt} &= sn\exp\{-\frac{E_{T_e}}{kT}\} - a_{T_e}n_c(N-n) - a_R n_c m \\
\frac{dn}{dt} &= -sn\exp\{-\frac{E_{T_e}}{kT}\} + a_{T_e}n_c(N-n) \\
\frac{dm}{dt} &= a_R n_c m = -I_{TL}(t)
\end{aligned} \tag{2.2}$$

where $n+n_c=m$ is the neutrality condition, a_{T_e} and a_R are the transition probabilities for trapping and recombination and I_{TL} is the thermoluminescence intensity.

Equations (2.2) are non linear differential equations that cannot be decoupled and have no known closed-form solution. In order to solve them, some approximations must be made by applying the quasi-equilibrium condition. Here, the population of electrons in the conduction band, and changes in this population, are considered small in comparison to the population of electrons in the trap T_e and any change in this population ($n_c << n$ and $\frac{dn_c}{dt} << \frac{dn}{dt}$). This results in the quasi-stationary solution for the rate of recombination:

$$I(t) = -\frac{dm}{dt} \simeq sn\exp\{-\frac{E_{T_e}}{kT}\}(1-\frac{a_{T_e}n_c(N-n)}{a_{T_e}n_c(N-n)+a_Rn_cm}) \tag{2.3}$$

This is known as the "general one-trap" expression for TL emission.[28],[29]

If the rate of retrapping of charge carriers into the charge trap T_e is small in comparison to the rate of recombination at the recombination center R ($a_{T_e}n_c(N-n) << a_Rn_cm$), then the thermoluminescence measured from the sample at a particular temperature T becomes:

$$I(t) \simeq -\frac{dn}{dt} \simeq sn\exp\{-\frac{E_{T_e}}{kT}\} \tag{2.4}$$

From equation (2.1), the intensity of the TL as a function of time can be related to the intensity as a function of temperature. Integration of equation (2.4) from $T=T_0$ to the final temperature results in the well known Randall-Wilkins function[30][31] for first-order kinetics:

$$I[T] = sn_o\exp\{-\frac{E}{kt}\}\exp\{\frac{s}{\beta}\int_{T_o}^{T}\exp(-\frac{E_{T_e}}{k\theta})d\theta\} \tag{2.5}$$

n_o is the initial concentration of the trapped charge at temperature T_o, and θ is a dummy integration variable that represents the incrementing temperature.

Each trapping center will have a different thermal depth and a different 'glow peak' associated with it. Heating over an extended range will often reveal the presence of several glow peaks.

2.1.2 Experimental Setup for TL

The sample was placed on a metal planchet which could be heated using electrical heaters. Cooling of the sample was done using liquid nitrogen which was forced through the metal planchet using a pump from Biorad. Control of the heaters, nitrogen pump, and temperature monitoring was performed by an Omega fuzzy logic controller with autotuning. Heaters used for heating were 50W 'firerod' heaters from Watlow. Measurement of the luminscence was done using a 9635 QB bialkali PMT from Electron Tubes, inc. For measurements which monitor the TL emission from F centers, colored interference filters with center transmission at 420nm and FWHM of 10 nm from Corion were employed to filter the TL emission from other light. For the luminescence spectra measurements, an Oriel model 77320 monochromator with a 1600 line/mm grating blazed at 500 nm was used to separate the luminescence spectra during TL.

2.1.3 TL Experimental Results

Typical TL curves from Al_2O_3:C are shown in figure 2.3. The samples were irradiated with 0.18 Gy $^{90}Sr/^{90}Y$ before the 200-550 K measurement and were irradiated with 200 Gy $^{90}Sr/^{90}Y$ before the 300-900 K measurement. Several distinct TL peaks are seen in these samples, of various amplitudes, one at ~260 K, ~310 K , ~450 K, respectively at 0.2

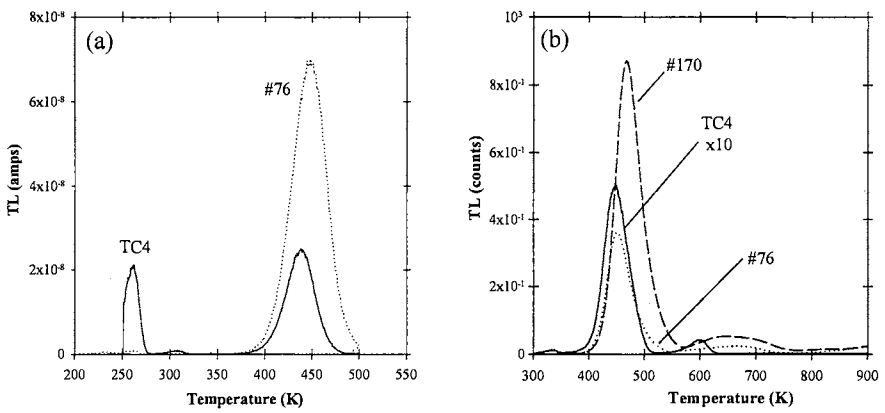

Figure 2.3 TL glow curves on three samples. Figure (a) shows the TL from samples TC4 and 76 over the temperature range of 200 K - 550 K. The dose delivered was to each sample was 0.18 Gy ^{60}Co and the heating rate used was 0.2 Ks^{-1}. Figure (b) shows the TL from samples TC4, 76, and 170 over the temperature range of 300 K - 900 K. The dose delivered to each sample was 200 Gy $^{90}Sr/^{90}Y$ and the heating rate used was 1.0 Ks^{-1}.

Ks^{-1} in Figure (2.3a). Figure (2.3b) shows a small peak at ~330 K, a larger peak at ~450 K, and small peaks at 600-650 K and the tail of a peak around 900 K. The 450 K TL peak is commonly referred to as the 'main dosimetric' peak because of its use in personal dosimetry. Around 450K and above, the TL suffers from a phenomenon known as thermal quenching of the luminescence center[2] which distorts the shape of this peak. The TL peaks at higher temperatures, such as 600 K and 923 K are heavily quenched. Comparison of this data with the TSC of Figure 2.7 indicate that the 600K and 900K trapping centers trap huge quantities of charge, yet the quenching is apparently so strong that little TL is seen. Recent evidence, however, indicates that much of the charge liberated from these traps does not recombine with the F center.[3]

---

2 See chapter 4 for more information

3 See chapter 5 for more information.

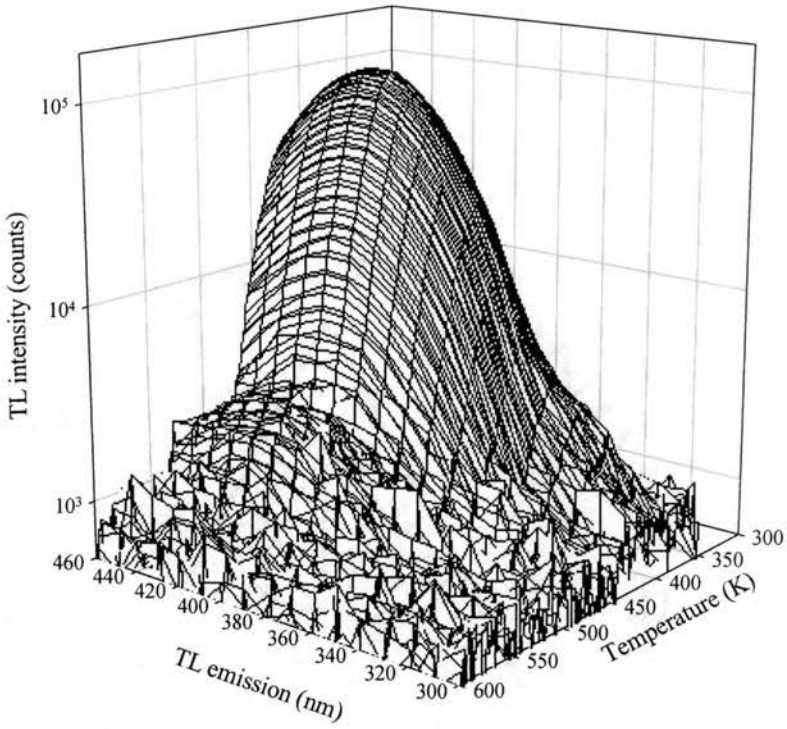

Figure 2.4 3D TL emission from sample 76. The emission from the 450K TL peak is seen to be centered at the F center (420 nm). There is perhaps some small contribution from the F^+ center (330 nm). Also seen is a much less intense F emission TL peak at 573K.

Figure 2.4 shows contour plots of the TL emission spectra from sample 170 between the wavelengths of 300 nm-460 nm. In the non-magnesium-doped samples, two TL peaks are seen, one at 450 K and one at 500 K. It is readily seen that the TL emitted from these samples, within the experimental limit of light detection, occur from the F center (420nm) emission. At 450 K, there appears to be perhaps some minor F^+ TL emission, but in any event, it is more than an order of magnitude less than the F center TL emission.

Figure 2.5 shows the TL spectral emission form an Al_2O_3 sample doped with magnesium (Al_2O_3:C,Mg). The resulting TL emission shows the usual 450K TL peak at the emission wavelength of 420 nm (note: the heating rate on these measurements was very

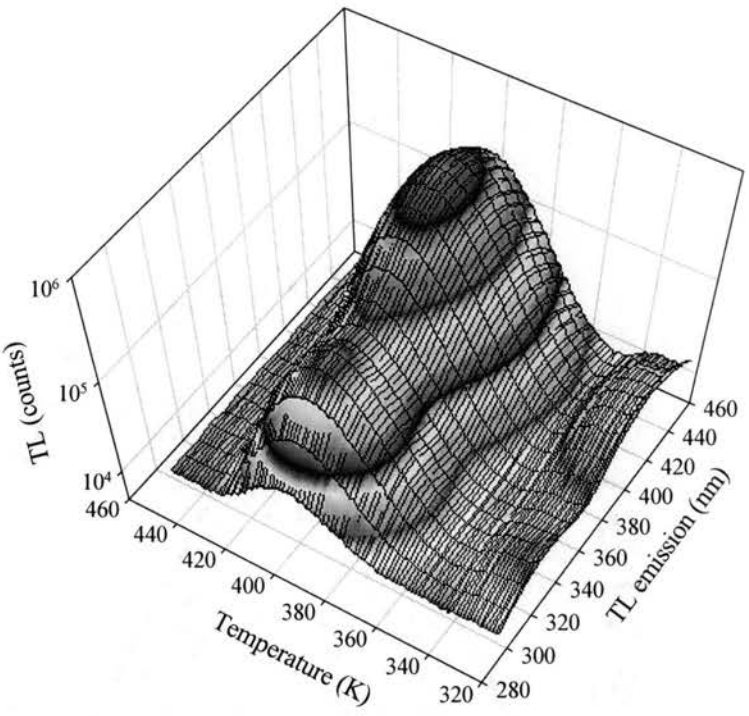

Figure 2.5 3D TL emission from magnesium doped Al_2O_3. The emission from the 400K TL peak is seen to be centered at the F center (420 nm) but there is in addition a very strong emission from the F^+ center at 330nm at the same temperature. There are also some TL peaks near room 300 K with emissions at both the F and F^+ center

slow which causes the TL peak to shift to the lower temperature of 400K). In addition to this TL peak, there is a strong TL emission F^+ center at 330 nm. Also seen are TL emissions at 300C which exhibit both F and F^+ emission at the same temperatures.

2.2 Thermal Processes: Thermally Stimulated Conductivity

A closely related phenomenon to thermoluminescence is Thermally Stimulated Conductivity (TSC). Instead of measuring the luminescence emitted from the sample when the electron recombines with the recombination center, an electrical field is applied across the sample. Any electrons excited out of the trapping centers will reside in the conduction

band for a short, but finite time. During this time, the charges undergo movement associated with the potential bias across the sample. This movement leads to small but nevertheless measurable currents.

The expression connecting the conductivity ρ^{-1} of the sample to the concentration of charge carriers in the conduction band is:

$$\rho^{-1} = e\mu n_c \tag{2.6}$$

where e is the electric charge of an electron and μ is the mobility of the charge carrier. If an ohmic contact (essentially the contacts do not form a barrier) of area A are located on opposite faces of a sample, then the measured current at a bias potential of V can be related to the conductivity by:

$$I = \frac{VA}{\rho} \tag{2.7}$$

The temperature dependence of TSC in Al_2O_3 is very similar to the temperature dependence of the luminescence. The simple model describing TL in the previous section works very well for TSC. Any charge excited out of the trapping center must first pass through the conduction band before it recombines with the recombination center. The TSC forms peaks of the same shape as the TL but generally the TSC does not peak at the same temperature as the TL. The reason for this temperature shift is due to the temperature dependence of the mobility of the charge carriers.

Thus the equation for the TSC peaks is identical to the TL peaks with the exception that it includes conductivity, the size of the electrodes, and the mobility (through ρ^{-1}):

$$I[T] = \frac{VAs}{\rho} \exp\{-\frac{E}{kt}\} \exp\{\frac{s}{\beta} \int_{T_o}^{T} \exp(-\frac{E_{T_e}}{k\theta}) d\theta\} \tag{2.8}$$

TSC has several advantages over TL. It is a direct measurement of all charge excited into the delocalized bands, whereas the TL is an indirect method which measures only one recombination pathway. A second advantage to TSC over TL is that the TSC does not suffer from the thermal quenching of the luminescence center. The 450 K TSC peak will appear undistorted, and the higher temperature peaks are easily seen. One disadvantage of TSC is that at appropriately high temperatures, ionic conductivity in the sample becomes so large that any currents associated with charge detrapping becomes difficult to separate from the ionic conductivity.

2.2.1 TSC Experimental Setup

Electrodes

Electrodes of various metals were vacuum deposited onto the surface of the sample to form the electrodes used for the TSC measurements. One criterion that must be fulfilled by the electrode material is that it must be robust enough to resist scratching and have approximately unchanged electrical properties over the entire temperature range of the measurements. Materials tested as electrodes were gold, silver, nickel, palladium, platinum, titanium, graphite, and aluminum. Of these, nickel, palladium, platinum and titanium were resilient enough to stay on the sample and their electrical properties remained fairly constant over the temperature ranges of 300K-1000K. Palladium was most often used because of its almost constant optical transmission over the visible and UV wavelengths ranges. This is unimportant for TSC, but is of importance for PC measurements.

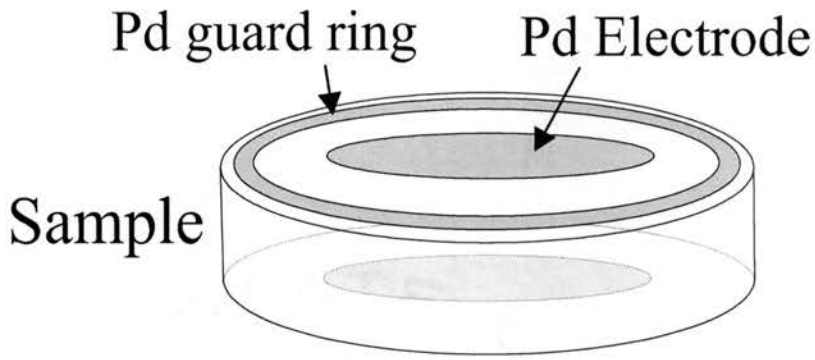

Figure 2.6 Schematic of the guard ring configuration used in TSC and PC measurements to minimize leakage currents. The sample size was 5mm wide x 1mm thick.

Since most of these samples served the dual function of being used in both TSC and PC measurements, the almost constant optical absorption proved the deciding factor.

The electrode was evaporated onto the sample into a guard ring configuration shown in fig.2.6, in order to minimize any leakage currents across the surface of the sample. When mounting the sample, care was taken to insure that the guard ring was grounded with respect to the current meter.

Sample holder and connections

The sample was mounted in a nickel holder that could be heated to 1000K. Spring loaded gold probes were used to ensure a connection to the electrodes on both faces of the sample. A Keithley 617 multimeter was used to supply the bias current applied across sample. Typical voltages of 100V were used to bias the sample. The Keithley 617 was also used to measure the TSC currents, which were internally averaged over 300 ms.

Temperature control

Temperature control was perfomed using an Omega CN 4800 fuzzy logic controller to control the output power to the heaters. Three 50W firerod heaters from Watlow were used to heat the nickel holder. Temperature measurement was performed using either K or E type thermocouples. The emf of these thermocouples was measured with a multimeter in conjunction to an icepoint and then converted into a temperature.

Irradiations

Irradiations of the samples were performed using either a $^{90}Sr/^{90}Y$ beta source delivering 6.79 $mGys^{-1}$, or a ^{60}Co source delivering 14.59 $mGys^{-1}$

2.2.2 TSC results

Figure 2.7 shows results from TSC measurements on the same three Al_2O_3 samples as discussed earlier. In these measurements, three distinct peaks can be seen, the main trapping center at 450 K, another trapping center at 573 K and a deep trapping center at about 973 K. Since the height of the peak is a reflection of the concentration of charge in a trap, one can see that both the 573 K peak and the 973 K peak hold a large amount of trapped charge in comparison to the main trap.

Comparing figures 2.3(b) and 2.7, the advantages of TSC over TL become apparent. The TL from the 573 K and 973 K TL traps is much smaller than the 450 K trap. However, the TSC indicates that there is a much greater population of charges released from these

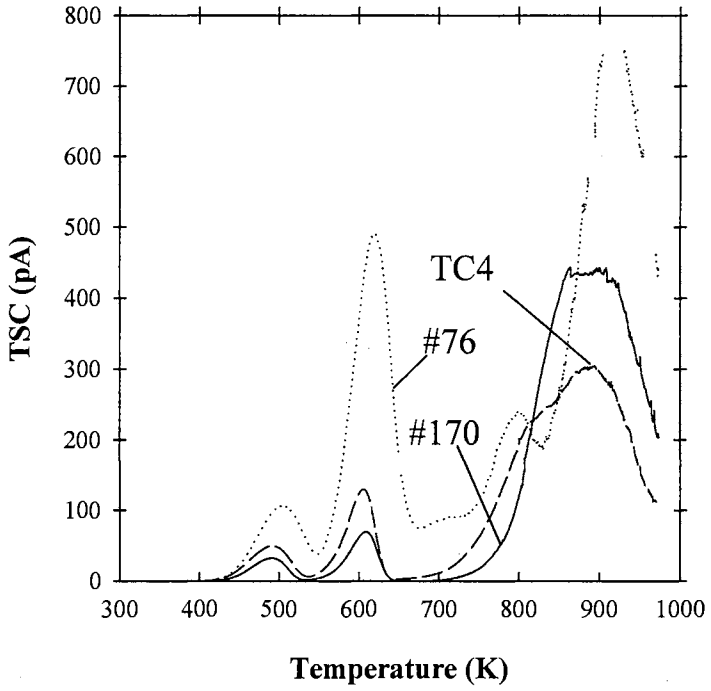

Figure 2.7 TSC curves from three samples showing the variation in concentration of trapping centers. The data were obtained using a bias voltage of 100V and a heating rate of $1.0Ks^{-1}$. The dose delivered to each sample was 300 Gy from a $^{90}Sr/^{90}Y$ source

traps than the 450 K trap. The difference id due to thermal quenching of the F center 420 nm emission (see chapter 3).

2.3 Optical Processes: Optically Stimulated Luminescence

2.3.1 Introduction to OSL: Simple model

One of the simplest models by which OSL can be produced in Al_2O_3 is shown in figure 2.8. This model consists of one light sensitive electron trap T, and one radiative recom-

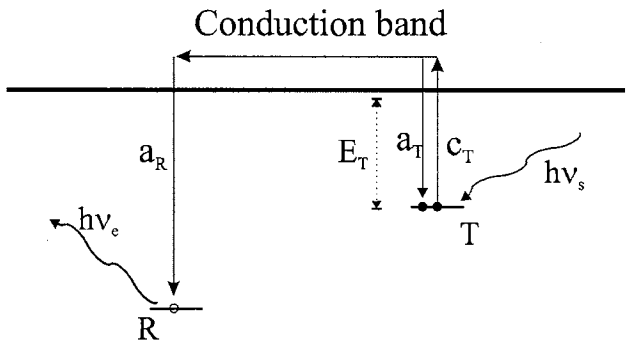

Figure 2.8 Schematic of a simple one trap OSL process. The incident stimulation energy $h\nu_s$ releases and electron from the trap T, which then recombines with the recombination center R, releasing a photon of energy $h\nu_e$.

bination center R, and the conduction band. In this model, the stimulation light of energy $h\upsilon_s$ excites the trapped electrons of concentration n into the conduction band at a rate c. These excited electrons then recombine with the trapped holes of concentration m at the recombination center. This recombination releases photons of energy $h\nu_e$.

The rate equation describing the flow of charges in this scenerio is:

$$\begin{aligned} \frac{dn_c}{dt} &= cn - a_T n_c(N-n) - a_R n_c m \\ \frac{dn}{dt} &= -cn + a_T n_c(N-n) \\ \frac{dm}{dt} &= -a_R n_c m \\ m &= n_c + n \quad \text{neutrality condition} \end{aligned} \tag{2.9}$$

Here, n_c is the number of electrons in the conduction band, a_R and a_T are the transition constants, related to the capture cross-sections by $a_{R,T} = \upsilon\sigma_{R,T}$, repectively, where υ is the thermal velocity, and N is the number of available states in trap T. c is the excitation rate, which is given by the product of the excitation intensity ϕ and the photoionization cross section σ ($c = \phi\sigma$). The photoionization cross-section is dependent upon the stimulation

energy ($\sigma[h\nu_s]$)[4] and therefore implies that the excitation rate will also be dependent on the stimulation energy ($c[h\nu_s]$)

The rate of recombination of electrons in the recombination center R is equal to the intensity of the OSL in this model $I_{OSL}[t] = -\frac{dm}{dt}$. If one makes the assumption of a quasiequilibrium condition ($\frac{dn_c}{dt} << \frac{dn}{dt}$, $\frac{dm}{dt}$ and $n_c << n,m$) and assumes negligible retrapping ($a_R >> a_T$), then the OSL intensity becomes:

$$I_{OSL}[h\nu_s, t] = -\frac{dm}{dt} = -\frac{dn}{dt} = c[h\nu_s]n \tag{2.10}$$

to which the solution is often written:

$$I_{OSL}[h\nu, t] = n_0 c[h\nu_s] \exp\{-c[h\nu_s]t\} = I_0[h\nu_s] \exp\{-\frac{t}{\tau[h\nu_s]}\} \tag{2.11}$$

where n_0 is the initial population of electrons in trap T at time t=0, $I_0[h\nu]$ is the intial intensity at time t=0, and $\tau[h\nu] = \frac{1}{c[h\nu]}$ is the decay constant. The quasiequilibrium condition lets the I_{OSL} be expressed in another way[4]:

$$I_{OSL} = k_{OSL}\frac{n_c}{\tau} \tag{2.12}$$

where τ is the lifetime of the electron in the conduction band and k_{OSL} is the luminescence efficiency. The lifetime of the electron in the conduction band can be related to the stimulation rate by $c = \frac{1}{\tau}$.

If there is more than one optically active trap and retrapping is still negligeable, then the measured OSL intensity becomes:

$$I_{OSL}[h\nu_s, t] = \sum_i I_{0i}[h\nu_s] \exp\{-\frac{t}{\tau_i[h\nu_s]}\} \tag{2.13}$$

---

[4] The wavelength dependence will be discussed in more detail in chapter 4 and 5

where the summation is over all trapping states i.

2.3.2 Experimental setup

CW OSL measurements

A Spectra-Physics argon-ion laser was used as the stimulation source. The wavelength was tuned to the 514 nm line. The output power was measured with a Melles-Griot 30 W power meter. The OSL was measured with a Electron Tubes bialkali PMT in photon counting mode. The emission light was filtered from the stimulation source by two Corion 415Δ10nm interference filters. Counting was done using a National Instruments DAQ board with 16 bit counter.

OSL spectral measurements

An Oriel 50W halogen lamp was used as the stimulation source. The broadband emission from the halogen lamp was separated into its component wavelengths by use of a Spex 1681 monochromator and then focused onto the sample. The OSL emission from the sample was separated into its individual components with an ORIEL 77320 monochromator. The OSL was then measured with an Electron Tubes 9635 bialkali PMT in counting mode. Counting was done using a Stanford Research SR 430 multichannel scalar.

Irradiations

Irradiations of the samples were performed using either a ^{90}Sr/Y beta source delivering 6.79 mGys^{-1}, or a ^{60}Co source delivering 14.59 mGys^{-1}

2.3.3 OSL Experimental results

CW OSL

Figure 2.9 shows the decay of the F center OSL from Al_2O_3:C (points) irradiated with 100 Gy of $^{90}Sr/^{90}Y$ when stimulated with a constant power of continuous wave laser light (CW) as well as a fit of the data to the sum of three exponentials, with a lifetime of 1.22 s (solid line), 5.24 s (dashed line), and 24.0 s (dotted line), respectively. The sum of the three exponentials is represented by the solid line through the points and thus it is seen that Eq. 2.9 models the data quite well.

The reason for the three different contributions to the OSL is that there are at least three different charge traps being stimulated by the incident optical energy of 2.41eV. Each has a different lifetime because each trap has a different photoionization cross-section. Variations of either the stimulation power, stimulation energy, or both will result in different decay lifetimes of each component being measured. Thus, the exact lifetimes measured here are of little importance. Of more importance is the number of trapping states contributing to the OSL. This will be discussed in more depth in chapters 4 and 5.

Fig. 2.11 shows an isometric measurement of the OSL stimulation and emission spectra from an unirradiated sample. Here, one can see the 420 nm emission when stimulating the sample directly in the F-center absorption region,[13] peaking at 205 nm. Also seen is the F^+ emission at 328 nm when stimulating directly in the F^+ absorption region, with absorption maxima at 230 nm and 255 nm. Fig. 2.10 shows a similar isometric measurement of the OSL stimulation and emission spectra, but from an irradiated sample. Once

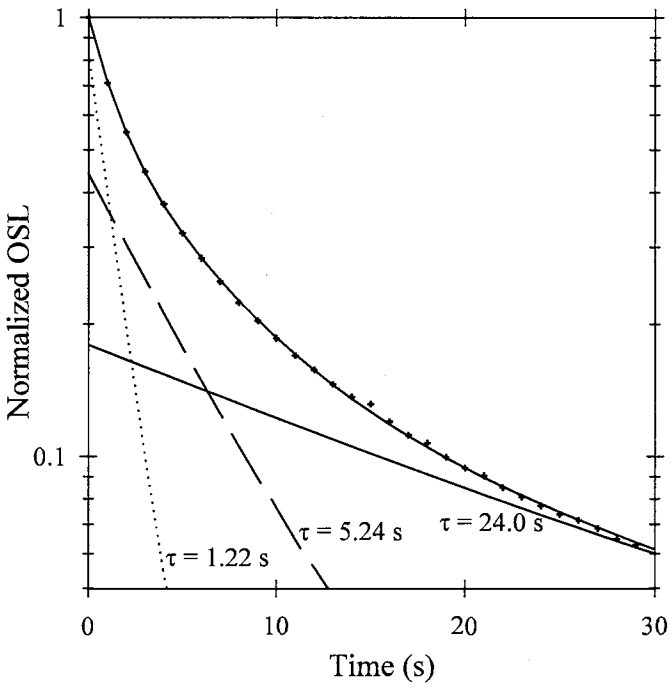

Figure 2.9 Decay of F center OSL under 1W of CW stimulation. Three decaying exponentials were fit to the data with lifetimes of 1.22 s, 5.24 s, and 24.0 s respectively.

again, one can see emission from the F and F^+ centers when stimulated at 205 nm and 328 nm respectively. However, we now see an emission shoulder peaking around 420 nm with a stimulation band that extends to longer wavelengths. The stimulation spectrum in Fig. 4 was only taken to 320 nm. However, measurements at a fixed emission wavelength (see Fig. 5 below) indicate that this radiation-induced shoulder, peak emission at 420 nm, is observed for stimulation wavelengths down to ~600 nm. Other workers have reported weak OSL when stimulating in the infrared[37] and thus it is expected that the stimulation shoulder will extend all the way to the red/infrared region of the stimulation spectrum. This results in a vast range of stimulation sources being used to excite OSL in Al_2O_3:C from halogen lamps, to CW argon-ion lasers to Nd:YAG and frequency doubled Nd:YAG lasers to infrared sources.[35],[36]-[37] It should be noted that since two different samples were used in these experiments direct comparison of the OSL intensities in Figs.2.11and 2.10 is not possible. One also sees in Fig.2.10 the presence of a comparatively weak emission centered around 500 nm when stimulating at ~300 nm. This is thought to arise from interstitial aluminum ions[?]. Lee et al.[14] saw an identical behavior in regular Al_2O_3 when neutron irradiated. Neutron irradiation tends to displace atoms from their lattice position more than other types of irradiation. This would, then, tend to support the conclusion that intersticial aluminum atoms are responsible for the 500nm emission.

The edges of peaks occuring at an emission of 350 nm with a stimulation maximum occuring at 255 nm and 230 nm is the edge of the F^+ emission The entire F+ stimulation-emission spectra can be seen in fig2.12. Here the F^+ center emission centered at 330nm

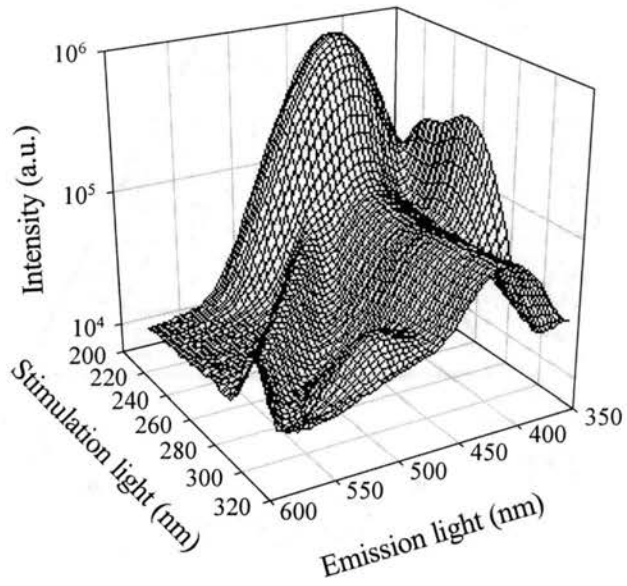

Figure 2.10 Isometric plot of the stimulation and emission spectra from sample 170. In addition to strong intrinsic F and F^+ emissions a wide stimulation band stretching from low wavelengths up to the limit of the current measurements (320 nm) is clearly evident. Additionally, green emission related to Al intersticials is seen at ~500 nm when stimulated at ~300 nm.

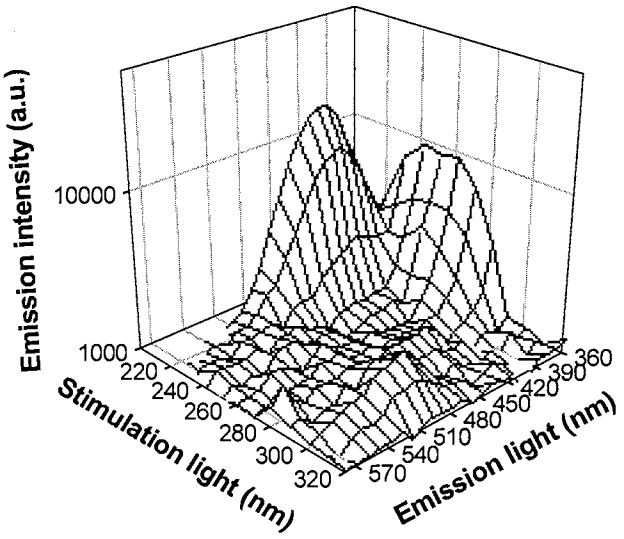

Figure 2.11 Isometric plot of the stimulation and emission spectra from an unirradiated Al_2O_3:C sample (sample #71). Emission peaking at 420 nm from the relaxation of excited F centers with maximum emission occurring for stimulation at 205 nm.. The large shoulder which appears for stimulation wavelengths between 220 nm and 280 nm is due to the relaxation of excited F^+ centers. Peak emission for the F^+ centers occurs outside the range of the measurement, at 330 nm. Emission maxima are observed at stimulation wavelengths of 230 nm and 250nm.

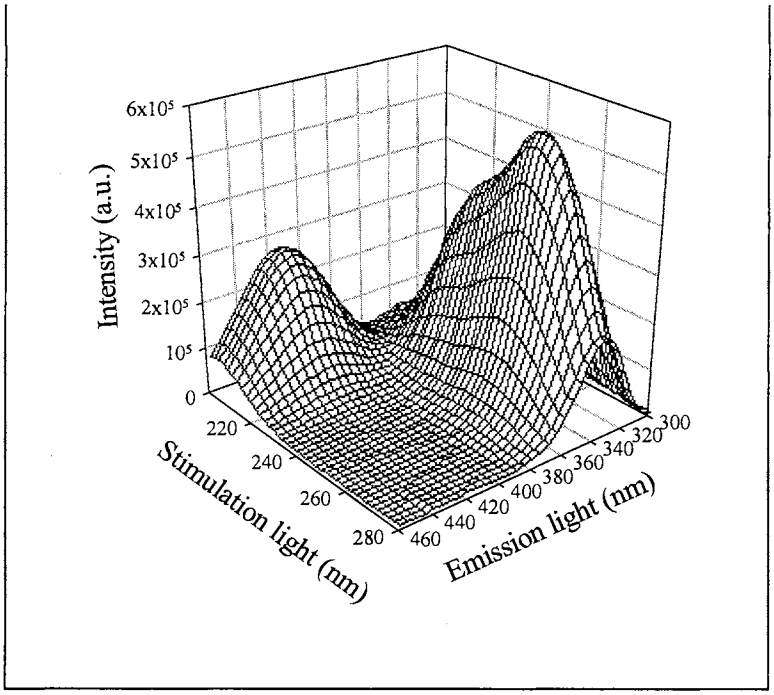

Figure 2.12 Isometric plots showing the emission of Al_2O_3:C over the region of 300-460 nm when stimulated with light in the wavelength range of 200-280 nm.

is seen to peak when stimulated with ~ 255 nm and 230 nm light. There is a shoulder extending into the 200 nm region but no strong peak occurs in this region. The F center emission centered at 420 nm is seen when the stimulation light is ~ 205 nm.

2.4 Optical phenomenon: Photoconductivity

2.4.1 Introduction to Photoconductivity

A closely related phenomenon to OSL is photoconductivity (PC). A light source is used to excite trapped electrons out of their trapping centers. However, as in the case of TSC, a bias potential is applied across the sample and instead of measuring the luminescence

emitted from the sample when the electron recombines with the recombination center, small currents associated with charge excited into the conduction band are measured.

This method has the advantage of directly measuring all the charge excited into the conduction band regardless of the recombination point. OSL, however, only indirectly measures one recombination pathway–the luminescent pathway of the particular optical recombination center that is being monitored.

The simple one trap-one recombination center model for PC can be shown to be proportional to the OSL model. The for the one trap-one recombination center case, the photoconductivity is:

$$I_{PC} = k_{pc} n_c e \mu V \tag{2.14}$$

where k_{pc} is efficiency of light absorption by the trapped charge carriers, μ is the mobility and V is the applied bias. Rearranging equation (2.12), the photoconductivity can be expressed as:

$$I_{PC} = \frac{k_{pc}}{k_{OSL}} I_{OSL} e \mu V \tau \tag{2.15}$$

As long as both μ, V, and τ are constants, then $I_{PC} \propto I_{OSL}$.

2.4.2 Experimental results

Generally, a PC measurement using a constant stimulation power on Al_2O_3:C results in a series of exponential decay curves very similar to the CW OSL shown in figure 2.9 since several charge traps are known to contribute to both the OSL and PC under optical stimulation. One PC measurement alone does not reveal any more information than an OSL measurement. However, if both the OSL and PC can be measured at the same time, then

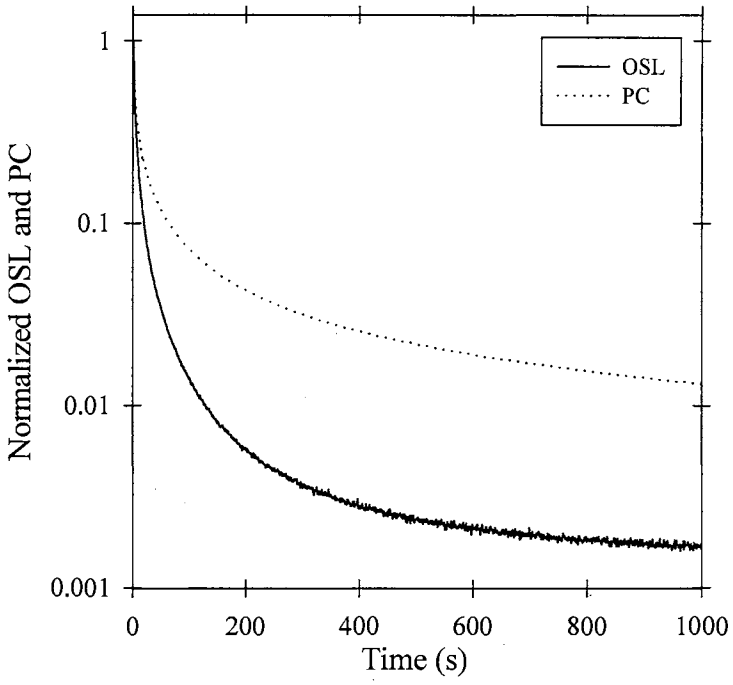

Figure 2.13 Simultaneous decay of both OSL and PC on sample 76. The sample was irradiated with 100 Gy of $^{90}Sr/^{90}Y$ before measurement. A bias voltage of 100 V was applied across the surface of the sample. The positive electrode was illuminated.

a good deal more information about charge recombination can be obtained than just from measuring each independently.

Figure 2.13 shows a simultaneous measurement of both PC and OSL decay on sample 76 irradiated with 100 Gy $^{09}Sr/^{90}Y$. The most obvious feature is that the normalized OSL decay is not identical to the normalized PC decay. This indicates the presence of charge in the conduction band that is not recombining with the OSL center (F emission in this case) that was being monitored. This will be discussed in more detail in chapter 5.

A problem with PC in Al_2O_3 is a buildup of static charge potential with time that points in the opposite direction as the applied DC potential. In Figure 2.14, a CW PC

decay is shown using a stimulation of 150 mW of 3.4 eV light. A constant bias of 100 V is applied to the sample for 100 seconds and the decay of the PC is measured. After 100 seconds, the bias was changed to -100 V without blocking the illumination of the sample. No data was taken for 10 seconds after the polarity change to allow for system relaxation, then data was taken for another 100 seconds. Photocurrents measured using a negative bias were negative. In order to compare the decays of the photoconductivity using both positive and negative biases, the absolute value of the data were used.

Fig.2.14 clearly shows that the data taken just after a bias change is considerably larger than data taken just before the bias change. Continuation of this process over a longer period of time reveals that the average value of each of the 100 second measurements of the PC is decaying almost exponentially. The straight line through the data points represents a fit of this data to a simple decaying exponential resulting in an average lifetime of this decay of 1940 seconds. Careful inspection of fig.2.14 reveals that this single decaying exponential is not a perfect fit to the averages of the photoconductivity. If the data acquisition time is extended beyond 2000 seconds, at least two decaying exponentials are needed to fit the the decay of the average lifetime of the photoconductivity.

The reason that a bias change results in an large initial increase followed by a decay is as follows. As charges are excited by the stimulation source, they are driven across the sample by the bias potential. This movement leads to a build-up of a static potential pointing in the opposite direction as the applied potential. This effectively lowers the total effective potential bias across the sample and leads to an overall decrease in the measured photoconductivity. When the applied bias is reversed, however, initially both the applied

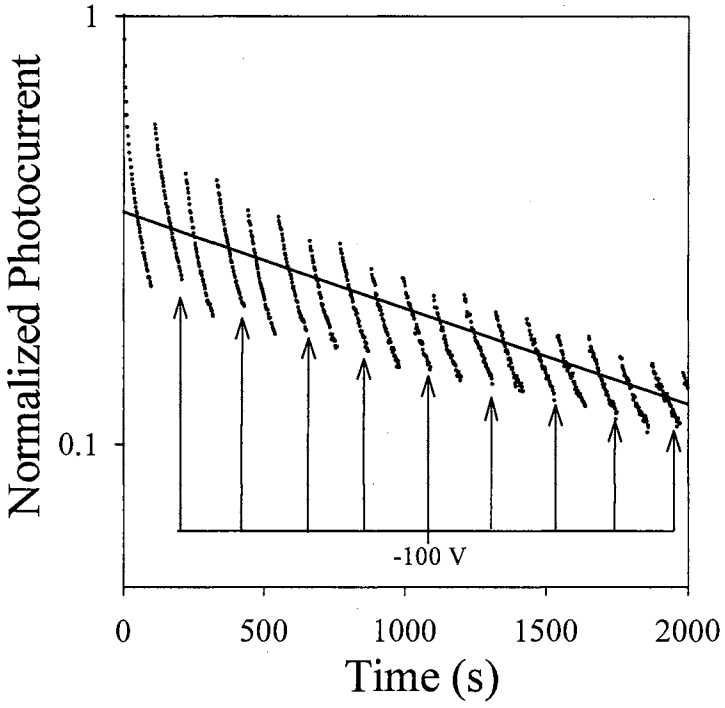

Figure 2.14 Decay of the photoconductivity of sample 76 using an alternating bias. For 100 seconds, 100 V was applied across the sample, then the voltage was reversed for the next 100 seconds. Arrows point to the photoconductivity under negative bias, the remaining curves used a positive bias.

bias and the static bias are pointing the same direction resulting in an overall increase in the effective potential across the sample. As the charges move through the sample, the static charge initially decreases and then starts to increase in the opposite direction again, leading to another static charge buildup pointing in the opposite direction to the previous static potential.

The cause of this space charge buildup could be due to (i) blocking at the electrodes, or (ii) charge trapping in deeper traps which are not efficiently emptied by the stimulation light. Fig.2.15 shows the dependence of the photoconductivity on the bias voltage using sample 76 and palladium electrodes. If the charge buildup was due to blocking at one of the electrodes, the voltage dependence of the photoconductivity would not be linear across the entire bias region. The photoconductivity, though, is clearly linearly dependent on the voltage which indicates that blocking due to only one electrode is not a problem. If both electrodes equally block charge, then the I-V plot would indeed be linear. If the charge is being retrapped in deeper traps that are no efficiently emptied, one would again expect a linear I-V plot. It is currently unknown which of the two possibilities leads to the buildup of a static space charge or if both ways contribute.

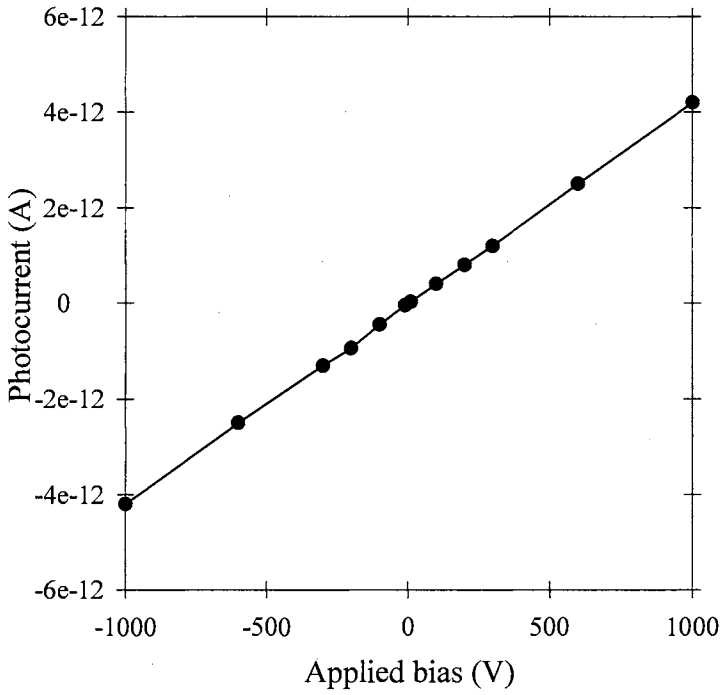

Figure 2.15 Dependency of the photoconductivity on bias voltage. The straight line through the data shows that the photoconductivity is linearly dependent on the bias voltage.

Chapter 3
THERMAL QUENCHING OF LUMINESCENCE CENTERS

3.1 Thermal quenching of F centers

3.1.1 Introduction

A property of the thermoluminescence properties of Al_2O_3:C is a strong heating rate dependence on the TL output.[38]-[41] With an increase in heating rate from 1 Ks^{-1} to 10 Ks^{-1} the total light output decreases four times.[38] The kinetics of TL production do not predict such a change. Instead, the total light sum is expected to be independent of the heating rate.[27] Furthermore, different heating rate dependencies have been found for crystals grown using different techniques.[42]

Several attempts have been made to model the behaviour of the TL glow curve from this material, using standard expressions for the TL glow peak shape. [40],[41],[43],[44] These analyses have resulted in large discrepancies between the calculated kinetic parameters for TL from this material, including the number of individual glow peaks present in the samples, the order of the kinetics, and the values for the activation energies and frequency factors. Little consensus was ever achieved when using only the standard TL expressions (eq.(2.5)).

Initial attempts to explain these observations centered on the proposal that they are the result of thermal quenching of the luminescence efficiency from the F centers.[45] This proposal was supported by the observation of a strong decrease in the intensity of x-ray induced radio-luminescence over the same temperature range as the TL is produced. [41],[44],[45] Several authors have applied the theory of Mott and Seitz to the radioluminescence-versus-temperature data in order to evalute the activation energy W and the frequency factor ν for thermal quenching of the F-center luminescence (see eq.(3.2)).

However, an apparent difficulty with this approach is that the shape of the radioluminescence-versus-temperature curve varies from sample to sample and depends upon the details of the heating (or cooling) cycle. This prompted Milman et al[44] to suggest a combination of processes to be responsible for the effects observed, including F center luminescence quenching and an "external quenching" process related to lattice relaxation effects as described by Gimadova et al.[42] and Avvakumova et al.[46]. In a more recent study,[47] it was observed that the variation of the TL intensity with the heating rate in Al_2O_3:C is dependent upon the degree to which deep traps are filled. Deep traps are thermally stable at temperatures at which the main TL signal is measured and it was observed that when the deep traps are prefilled (using a large radiation dose), the heating rate dependence of the main TL signal at 450 K is altered dramatically. In addition, using a fractional glow technique (FGT), the variation in the TL activation energy E_a with temperature was found to depend upon the degree of deep trap filling.[47],[48] This prompted Milman et al.[47] to declare that the heating rate dependence of TL from this material was not the result of thermal quenching and to propose instead a temperature-dependent competition process in

which the radiative recombination centers compete with deep traps for the localization of electrons during TL readout. It was suggested that the deep traps compete more effectively at higher temperatures and, thus, as the sample is heated during the TL measurement, more trapping in the deep traps take place. Since the TL emission shifts to higher temperatures at a higher heating rate, a reduced TL output is expected to be observed at higher heating rates due to this competition effect. If the deep traps are prefilled, though, they are less effective as competitiors and the heating rate dependence is altered. This idea was supported by Kulis et. al.[48] who also observed a dependence of the FGT E_a, and a variation in the radioluminescence temperature dependence with sample origin.

This lack of consensus regarding the mechanism(s) for the observed anomalous TL properties of Al_2O_3:C prompted this investigation into the thermal quenching effects on the F center photoluminescence. Presented are measurements of the F center photoluminescence lifetime that show the temperature depence of the F centers are entirely consistent with a classical Mott-Seitz temperature dependence. The parameters for thermal quenching obtained from these data (namely, W and ν) are seen to be independent of sample type, the heating or cooling rate, and the degree of deep trap filling.

3.1.2 Experimental Details

Samples

For this study, single crystals of Al_2O_3:C, 5mm in diameter and 1mm thick, supplied by Stillwater Sciences LLC. Some of the crystals used in the photoluminescence and TL measurements were polished on both sides and some were left unpolished. No significant

differences were found between the polished and unpolished samples. Each sample was grown under slightly different crystal growth conditions and were characterized by different concentrations of F and F^+ centers, and by having different TL glow-curve shapes. In particular, the main TL peak used at ~450 K was observed to be wider in some samples than in others, and the concentrations of shallow traps responsible for TL peaks at ~260 K and ~310 K were also observed to vary from sample to sample (see fig.2.3). A variety of samples was selected using these criteria in order to investigate the influence of the different F center and trap concentrations on the properties of thermal quenching of the F center luminescence. Before the experiments were carried out, all samples were annealed at 1173 K for 15 min in air, followed by cooling to room temperature outside the oven. Annealing at 1173 K insures that all charge is emptied from the trapping centers.

Luminescence lifetime

For UV excitation of the F center we used either a Xenon Corporation 457A "micropulser" xenon arc lamp with a 20 μs pulse width (full width at half maximum), or a Xenon Corporation "nanopulser" arc lamp with a 10 ns pulse width. For UV excitation of the F^+ center, a 50W Oriel deuterium lamp was used. The wavelength of the excitation band for both the F and F^+ stimulation was selected using a Spex Minimate monochromator with a typical bandwidth of 1.5 nm. The sample could be linearly heated or cooled over the range 300-600 K, with heating (or cooling) rates from 0.1 to $2Ks^{-1}$. Luminescence of the F center was detected through two Corion 420Δ10nm interference filters using an Electron Tubes 9635QB photomultiplier tube (PMT) operated at room temperature. Lu-

minescence of the F^+ center was detected by passing the emission light through an Oriel 77320 monochromater with a 1200 line-mm^{-1} grating blazed at 280nm. The PMT was operated in photon counting mode and data acquisition was performed using a Stanford Research SR430 multichannel scaler (MCS). Triggering of the flash lamp and the photon counter/scaler, and gating of the data acquisition were all synchronized using a pulse generator. The temperature of the sample holder was measured in the middle of each data acquisition period.

Irradiations

Irradiations of the samples were performed using either a $^{90}Sr/Y$ beta source delivering 6.79 $mGys^{-1}$, or a ^{60}Co source delivering 14.59 $mGys^{-1}$

3.1.3 Thermal quenching of Luminescence Lifetime

The standard Mott-Seitz model of thermal quenching[26] is represented in fig.3.1 Here, a configurational coordinate diagram is used to represent the electronic transitions between an excited state and a ground state within the same atom. At ground state, an electron will reside around the minimum energy point *A*. An electron absorbing incident radiation of energy E_a or greater will result in a transition from the ground state to the excited state, *B*, without an adjustment of the configurational coordinate (Frank-Condon principle). The ground state minimum and the excited state minimum in coordinate space are separated by an amount q_0. Thus the excited electron will lose some energy, dissipated as heat, in order to reach the excited state minumum at point *C*. At this point, the excited electron can recombine with the ground state by following the transition from *C* to *D*, releasing light

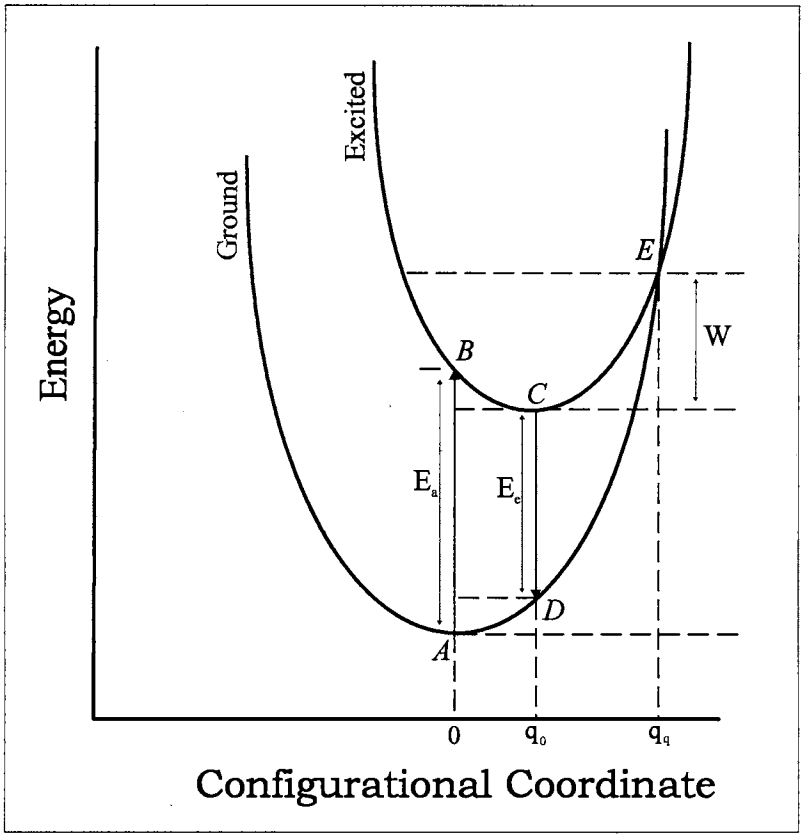

Figure 3.1 Configurational coordinate diagram of a luminescent center with potential energy curves for the excited and ground states as a function of the configurational coordinate. Adapted from McKeever [26]

of energy E_e. This is the normal luminescence recombination process. Notice that the emission energy E_e is less than the absorbed energy E_a. Hence, we would expect a Stokes shift between the absorbed luminescence and the emitted luminescence.

An additional route by which the excited electron can return to the ground state is shown in the configurational coordinate diagram. If the electron absorbs thermal energy of W while in the excited state, a transition from C to E can occur. From E, the electron can return to the ground state without the emission of radiation, but with the dissipation of

heat eventually leading to the return of the electron the vicinity of the minimum at A. This pathway is the thermal quenching pathway.

The total probability of decay from the excited state P_t is given by

$$P_t[T] = \frac{1}{\tau} = \frac{1}{\tau_0} + p\coth(\frac{\hbar\omega}{kT}) + \nu\exp(-\frac{W}{kT}) \tag{3.1}$$

where τ is the excited state lifetime, τ_0 is the radiative lifetime, p is a temperature-independent constant, ω is the phonon vibration frequency, $\hbar$ is Planck's constant, k is Boltzmann's constant, and T is temperature. W and ν are the activation energy and frequency factor, respectively for the nonradiative thermal quenching process. The middle term in eq.(3.1) accounts for the temperature dependence of the optical absorption of the sample. If we assume that the changes of the optical absorption due to a changing temperature are negligible over the temperature region used, then the luminescence decay time has the following temperature dependence:

$$\tau[T] = \frac{\tau_o}{1 + \tau_0\nu\exp(-\frac{W}{kT})} \tag{3.2}$$

Therefore, by measuring τ as a function of temperature and fitting the experimental data to Eq. (3.2), the parameters τ_o,W and ν for thermal quenching of the luminescence process can be obtained.

Typical luminescence decay curve following a pulse of UV light from the micropulser can be seen in Figure 3.2. The data displayed was taken by averaging over 100 pulses at room temperature . When the sample was excited in the F absorption band (205nm), and the emission monitored in the F emission band (420nm), the shape of the decay of the F

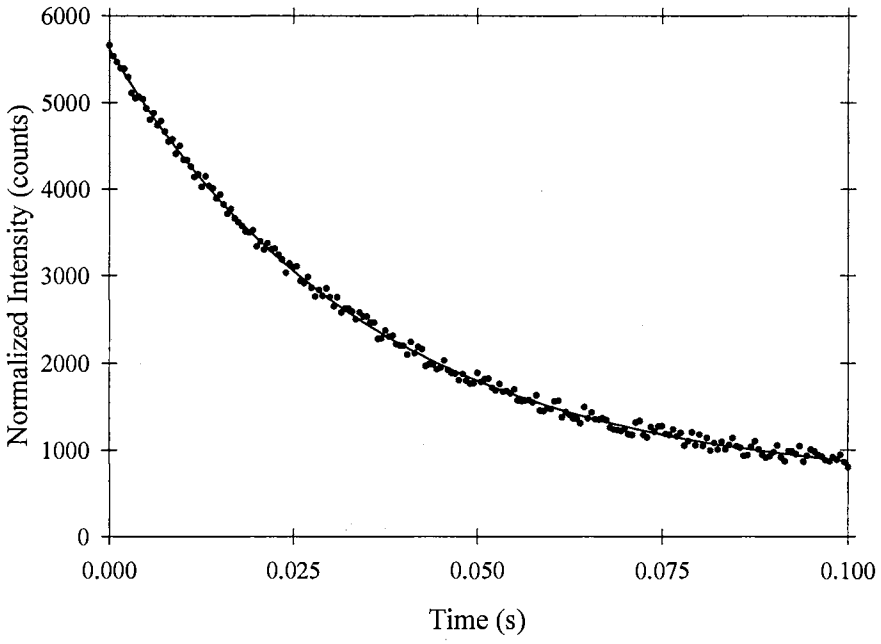

Figure 3.2 Photoluminescence decay curve in Al_2O_3 following pulsed excitation with 205nm light at room temperature. The solid line is the fit of the data to Equation with values of $I_o = 5030$, $\tau = 0.035s$, and $C = 580$.

emission could be modelled by:

$$I = I_o \exp(-\frac{t}{\tau}) + C \tag{3.3}$$

where I_o is the initial intensity, t is time, τ is the luminescence lifetime, and C is a constant luminescence offset. The solid line through the data points in Figure 3.2 is a fit of the data to eq.(3.3) with the parameters $I_o = 5030$, $\tau = 0.035s$, and $C = 580$.

3.1.4 Photoluminescence results

F center luminescence decay

Figure 3.3 shows the temperature dependence of the F center decay parameters. The data shown here are actually the temperature dependence of I_o, τ, and C, from eq.(3.3). The data were taken by measuring the decay of the F center luminescence at a particular temperature, as shown in fig.3.2, and fitting this decay to eq.(3.3).

One can readily see that the initial intensity has remained almost constant throughout the entire temperature range. However, both τ and C varied considerably as the temperature increased. The fact that I_o is not temperature dependent is not surprising. Since the number of F centers that are being directly stimulated by the 205 nm pulse is approximately constant throughout the temperature range used, the initial intensity I_o should also remain approximately constant.

The decay time τ of the exponential component reduces as the temperature increases, from a value of ~35 ms for all temperatures between room temperature and ~370 K, to less than 1 ms for temperatures greater than 485 K. Lee et al[14] measured the lifetime for the F center decay at room temperature to be 35 ms, which corresponds well with values obtained in these experiments. The solid line through the data in graph (B) shows a nonlinear regression analysis of the data using Eq. (3.2). Even though only one $\tau[T]$ curve is shown for one particular sample, many different samples were used resulting in the same temperature dependence in τ. The mean values determined from the regression analyses of all the data were $W = 1.08 \pm 0.03eV$ and $\nu = (1.02 \pm 0.84)\text{x}10^{14}$. For $\tau = \tau_o = 35ms$,

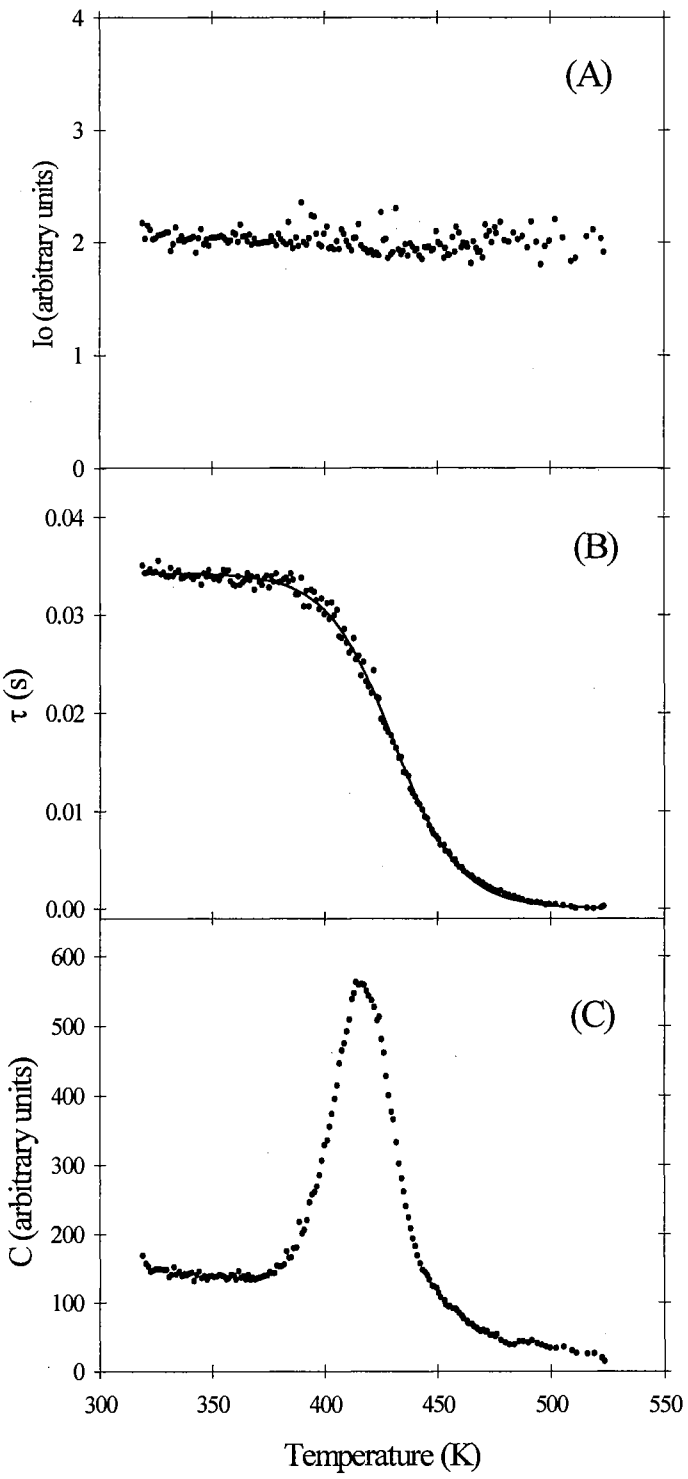

Figure 3.3 Fit of the F center decay in Al_2O_3:C at various temperatures to Eq. (3.2). Graph (A), (B), and (C) show the temperature dependence of I_o, τ, and C, respectively.

the dimensionless constant $\tau_o\nu = (3.6 \pm 2.9)\text{x}10^{12}$. These values are considerably lower than those reported elsewhere: $W = 1.55 - 1.56eV$ and $\tau_0\nu = (1-2)\text{x}10^{17}$. [40],[41]

The offset C is not actually a constant. It is also a slowly decaying luminescence signal which is temperature dependent. However, on the time scales that are shown here, this decay can be assumed to be an approximately constant. This slower decaying component is caused by the photoionization of the F centers and trapping of the photo-excited electrons by the various electron trapping states present in the material. Thermal depopulation of trapped charge then results in a phosphorescence component with a long lifetime, the value of which depends upon the energy and the frequency factor distributions of the traps and the temperature of the sample.

For the temperature ranges below 400 K, the phospherescence arises mostly from photo-excited electrons becoming trapped into the 260K trap, and then being thermally released. Above 400K, the temperature is such that any trapped charges in the main TL trap are thermally released, adding to the parameter C. As the temperature increases, more charge is thermally liberated from the main dosimetric trap and recombines with the F center. However, at some point, two things happen. Firstly, the population of the trapped charges decreases in the 'main' trap, which leads to a decrease in the constant offset. This is exactly the same phenomenon which leads to TL, and in fact, the parameter C has a TL peak shape in this region. Secondly, the thermal quenching of the luminescence lifetime leads to the decrease in this constant offset, as seen in the temperature region above 450 K. If it were not for the thermal quenching, the offset would not only have the phospherence contribution from the 260 K trap, but also there would be the contributions for the 'main'

TL trap. Thus, the constant offset would be expected to be even greater after the main TL trap than it was before.

There are cases in which the decay of the F center luminescence does not precisely follow the behaviour modelled by Eq. (3.3). Shown in fig.3.4 is the decay of the photostimulated F center luminescence at 348 K for sample TC4. This sample has a large concentration of 265 K traps in comparison to the concentration of traps at 450 K as can be seen from the TL shown in figure 2.3(a).

Each time a pulse of stimulation light excites the sample, some of the photoexcited electrons will become trapped into the shallow 265 K trap. In a sample like this, at room temperature,the lifetime of the electrons in the shallow trap is in the 300-700 ms range. On the timescale of the measurement (100ms), this is still rather long and thus this contribution only adds to the offset constant C. As the temperature increases, the lifetime of the charges in this shallow trap decreases considerably. Between 320 K and 360 K the lifetime of the phosphorescence process resulting from the thermal depopulation of the 265 K trap becomes comparable with the lifetime of the directly excited F centers and the concentration of thermally depopulated electrons is comparable with the concentration of photostimulated electrons. At these temperatures, the parameter C can no longer be considered a constant with respect to time. Eq. (3.3) is no longer a good approximation to this behavior and will consequently give erroniously large values for the luminescence lifetime of the F center.

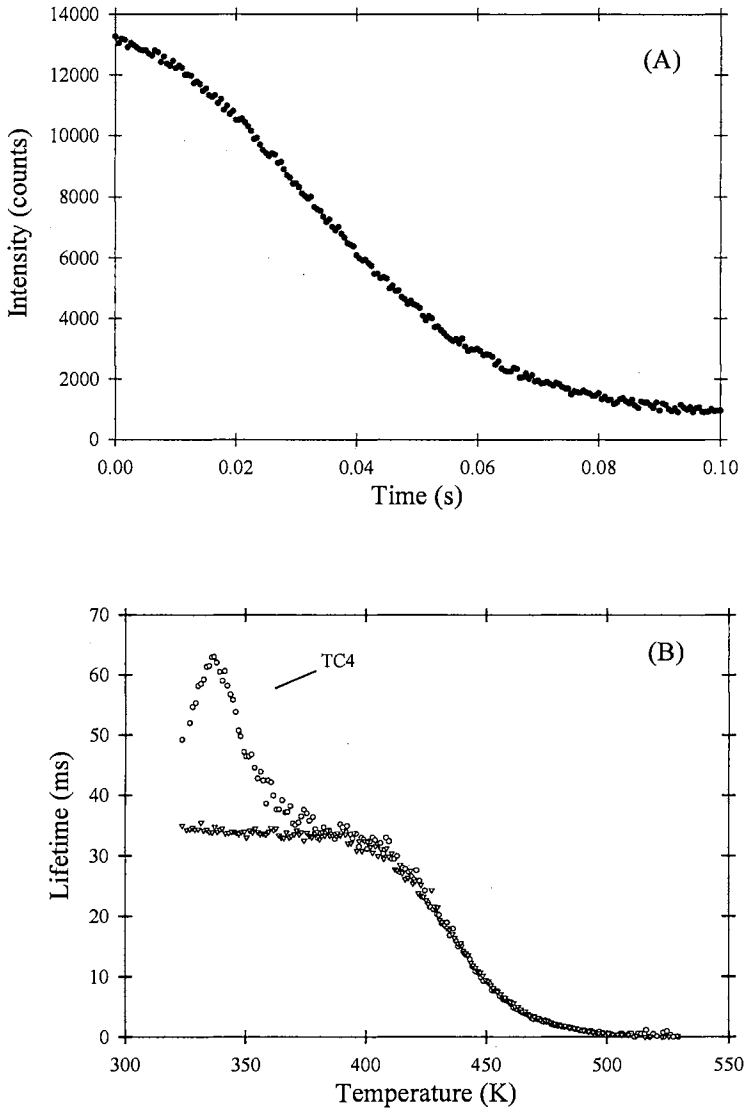

Figure 3.4 (A) The thermal depopulation of a large concentration of trapped electrons at ~260K distorts the decay of F center luminescence. Sample TC4 was at 348 K when these data were taken. (B) The effects of the shallow traps on the calculated lifetime of the F center luminescence using eq. 3.3

In some samples measured, the initial 10ms showed an increase in the F center luminescence followed by a decay. Indeed, depending on the temperature, the same sample might show an initial increase of the luminescence at one temperature and at another show a decay of the luminescence similar to fig.3.4. The exact shape of the measured F center decay in samples such as these varies considerably from sample to sample and from one temperature to another. The reason for this variation is that phosphorescence component at these temperatures is dependent on the concentration of 265K traps which vary considerably from sample to sample. McKeever et al.[49] found a very similar phenomenon in quartz in which they measured the decay of the OSL luminescence under CW excitation. The model developed by those authors should model the behavior seen here quite well. However, the interest of this experiment was to measure only the lifetime of the F center luminescence, not the lifetime of the F center and phosphorescence components combined. Thus, samples which resulted in decays which were not well modelled by Eq. (3.3) because of these shallow trap interactions were avoided.

Heating rate dependence of thermal quenching parameters

It was already mentioned[5] that the TL peak at 450K in Al_2O_3:C strongly depends on the heating rate. To test if the F center luminescent lifetime parameter had any dependence on the rate of heating during continuous warming and cooling of the sample, heating and cooling measurements were performed with linear ramps between 0.05 Ks^{-1} and 1.5 Ks^{-1}. It was found that within the precision of our temperature measurements ($\pm$0.5 K), there

[5] See section 3.1

was no significant change in the lifetime or the thermal quenching parameters W and ν for the different heating and cooling rates used.

Dependence on the degree of filling of the deep traps

Following the suggestion of Milman et al.[47], that the apparent quenching properties are a function of the degree of filling of the deep traps, investigations of the effects of filling the deep traps on the the parameters of the F center luminescence decay were undertaken. The samples were pre-exposed to a large dose of irradiation (158 Gy) and preheated to 523 K to empty the main 450 K traps. The luminescence lifetime was then measured as before, and the data compared with those obtained from a sample which had been freshly annealed at 1173 K to empty the deep traps. The results are shown in Figure 3.5 for two different samples and show that the decrease in the luminescence lifetime is entirely independent of the degree to which the deep traps are filled. This clearly demonstrates that the effects related to prefilling the deep traps reported by Milman et al. [47] are not related to the phenomenon of thermal quenching of the F center luminescence. Akselrod et al.[25] showed that they are, in fact, explained using the standard kinetics of TL production.

Luminescence intensity

The temperature dependence of the F center luminescence intensity in Al_2O_3:C was also measured during linear heating and cooling of the samples. If one measures an integrated luminescent signal (integrated over 1s) emitted by the sample under CW excitation at 205 nm instead of measuring the decay of the luminescence excited by pulsed stimulation, large differences in the temperature dependent integrated luminescent signal are seen.

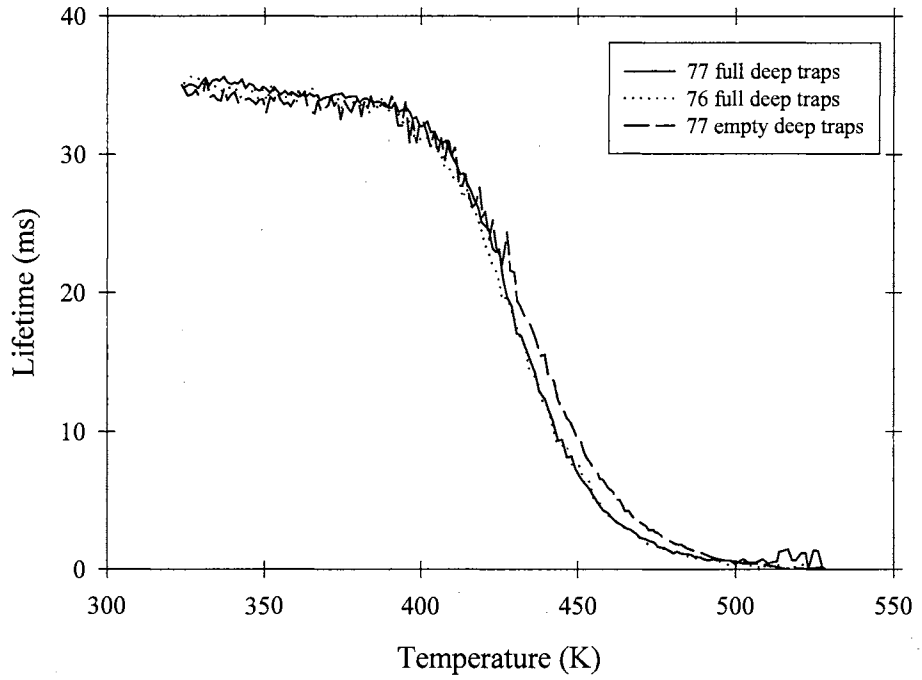

Figure 3.5 Effects of trap filling on the thermal quenching of F center luminescence.

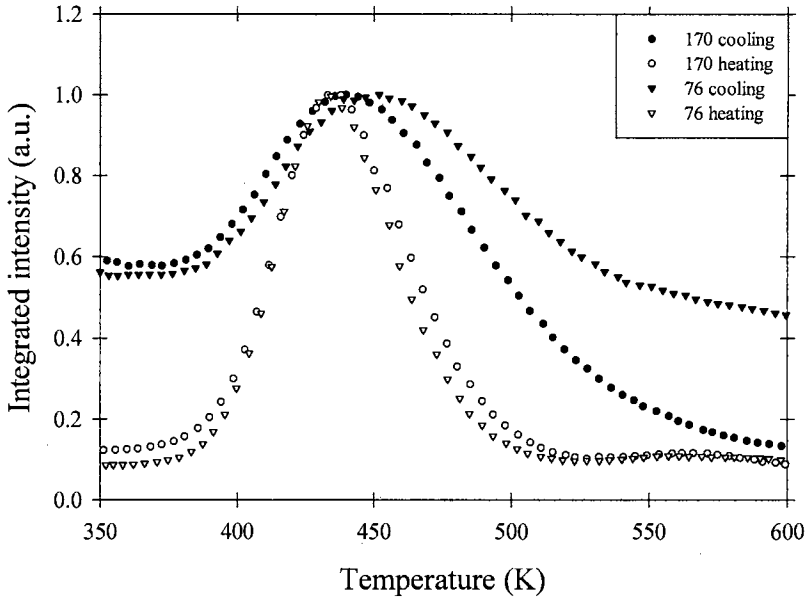

Figure 3.6 Integrated photoluminescence (over 1 second) as a function of temperature for samples 170 and 76. Shown is both the temperature depedence of the samples for both heating and cooling.

Such differences are illustrated in figure 3.6 The most obvious feature is that even though the $\tau[T]$ dependence of these two samples is identical to that shown in Figure 3.3 (B), the temperature dependence of the integrated luminescence of the two samples varies not only considerably from each other, but also varies depending upon whether the sample is being heated or cooled. The major reason for the differences in the behavior are caused by phosphorescence from the 450K traps. These data illustrate the main difficulty with measuring the luminescence intensity to monitor thermal quenching of luminescence–namely, the inability to separate quenching effects from thermally stimulated charge detrapping effects. By measuring the luminescence lifetime, however, such problems are overcome and

thermally stimulated quenching effects can be clearly separated due to their different time constants.

3.2 Thermal quenching of F+ centers

Measurements of the thermal quenching of the F^+ centers is not nearly as straightforward as the measurement of the F centers. As was discussed in the previous section on F center thermal quenching, the simplest approach to determine the thermal effects on the luminescence lifetime is to monitor the lifetime of the luminescence itself. Unfortunately, in the case of the F^+ center, direct measurements of the lifetime were not possible because the maximum lifetime of the luminescence is $\leq$ 7 ns.[13] The minimum pulse width of the nanopulser used to stimulate the F center was about 100 ns. Thus, there was no way to resolve the decay of the F^+ center from the stimulation source. Instead, a deuteurium lamp was used as a stimulation source in CW mode. The stimulation wavelength used to excite the F^+ centers was 250nm.

Considerable effort was spent in the previous sections explaining the thermal effects on the F center emission by measuring the integrated luminescence emitted from Al_2O_3:C gave very complicated, difficult to interperate data which was sample dependent. The main reason for this phenomenon, as was discussed, was because of the phospherescence associated with ionization of the F center leading to trapping/detrapping effects. Without these effects, the term C in eq.(3.3) would have been constant.

If the value of $C <<$ luminescence intensity, then it can be neglected from eq.(3.3) altogether. From figure 2.4, it seen that the F^+ center TL emission resulting from typical

Al_2O_3:C in the region of the main TL trap is several orders of magnitude smaller than the F center TL emission . In addition, in fig.2.12, the direct stimulation of the F^+ centers at 250nm shows that the intensity of the F^+ emission is larger than the direct stimulation of the F center at 205nm. Additionally, stimulation light at 250nm is not energetic enough to ionize the electron from the F^+ center. Taking all of this together, namely 1) the energy of the stimulation source is not enough to ionize electrons from the F^+ center to populate any of the thermal traps, which results in no trapped charge to contribute to the parameter C; 2) if there is any charge in the trapping centers, TL emission of the F^+ center is miniscule in comparison to the F center TL emission, resulting in very little effect by any phosphorescent component should there be one; and 3) the direct stimulation in the F^+ absorption region results in stronger emission than emission from the F center when stimulated in its absorption region, resulting in even less significance of the parameter C. These three factors taken together lead to the conclusion that the parameter C for the F^+ center emission is negligeable.

If this is the case, then the integrated luminescence intensity I can be related to the thermal quenching by:

$$I[T] = I_0 \varepsilon[T] \tag{3.4}$$

Here, ε is an efficiency factor that relates τ to τ_0 ($\varepsilon[\tau] = \frac{\tau}{\tau_0}$).

The assumption that the parameter C is small can be indirectly tested. From figure 3.6, the CW F center integrated intensity showed a rather large increase in temperature region of the main TL trap (450K). This is a result of the increase in C due to the phosphorescence contribution. The reason for this is that in the process of starting with an intially

low temperature, and heating the sample, the temperature of the sample is below the main TL trap for a considerable period of time. Electrons ionized from the F center can become stably trapped in the 450K trap, leading to a concentration buildup of charge in the trap as the measurement proceeds. As the temperature of the sample reaches the region of 450K, the electrons are thermally depopulated from the trap, resulting in a huge build up of the integrated F center emission intensity in this region which severly distorts the sigmoidal shape of the thermal quenching curve. If the F^+ emission shows a similar increase in the parameter C due to a phosphorescence component, a distortion of the thermal quenching curve would be seen in the 450 K region.

Figure 3.7 show the results of CW intensity measurements of the F^+ center when monitored at 330 nm. The samples were heated at a rate of 0.2 Ks^{-1}. The data for all three samples showed a very uniform thermal quenching effect on the F^+ center. Fits of the data to equation (3.4), and ultimately to (3.2), resulted in a determination of the average value for the activation energy $W = 0.602$ eV. The average value of the term $\tau_0\nu$ was determined to be 1.231x10^5. Since the lifetime of the F^+ center is currently unknown, an estimation of the frequency factor is not possible. However, the lifetime is known to be at maximum 7 ns,[14] which puts a minimum value on the frequency factor of $\nu \geq$1.75x10^{14} s^{-1}. There appears to be no distortion of the thermal quenching shape in the region of the main TL trap. Thus, the assumption that the effects of temperature dependent phosphorescent components are negligible in these measurements seems justified.

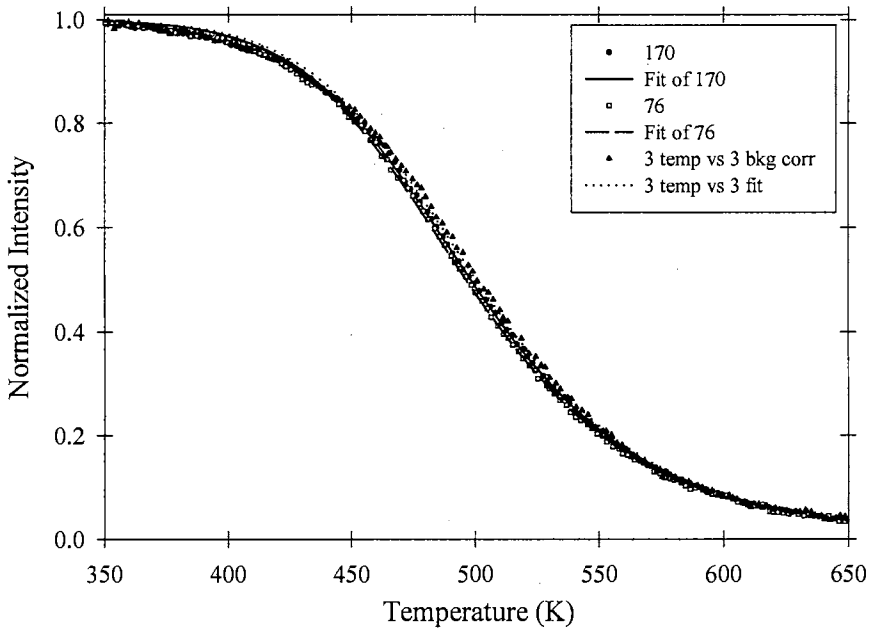

Figure 3.7 Thermal quenching of the F^+ luminescence in samples 170, 76 and 3. Samples 170 and 76 were obtained from Landauer, USA and sample 3 was obtained from Medus, Russia.

Chapter 4
PHOTOCONDUCTIVITY AND PHOTOIONIZATION CROSS-SECTIONS

4.1 Introduction

The OSL properties of this material are characterized by an optical stimulation band that extends over a very broad wavelength range from the UV region to the infrared (c.f. fig.2.10).[35],[36]-[37] Because of this broad stimulation region, one can use a large variety of stimulation sources ranging from various lasers to diodes to broadband lamps. These measurements were undertaken in order to better understand the optical depths and numbers of the various trapping centers which contribute to this broad OSL.

TL and TSC measurements indicate that there are several traps at a variety of trap depths. Recently, Agersnap Larsen *et al.*[52] attempted to determine the thermal trap depths of the localized states responsible for the TL/TSC signals. Using TSC over the temperature range of 340-650 K they found that two dominant energy states were responsible for the TSC signals in this temperature range. The states were also found to be distributed in energy, centered around 1.4 eV and 1.75 eV. A distribution of energy levels supports the data of Walker *et al.* [34] who studied the dose dependence of the 450 K TL peak. The behavior of this signal as a function of dose (*i.e.* the variation in the TL peak position as the dose increased) indicated that the peak is a composition of several, overlapping components. They also reported that exposing Al_2O_3:C to light will bleach the

TL/TSC traps. Since the thermal energy depths of the TL traps are distributed in energy, we may expect that the optical trap depths will also be distributions and not discrete values. The optical depths of the OSL traps are unknown but, since there are several TL traps, we should expect there to be several OSL traps, such that one expects a significant stimulation wavelength dependence of the OSL signal over a wide range of stimulation energies.

This chapter is primarily concerned with a measurement of the optical threshold energies for the traps, including the distributions in these energies, and the photoionization cross-sections. If we assume that both the photoconductivity and OSL proceed via charge transfer to the conduction band, then the optical depths and photoionization cross-sections can be determined from a measurement of either the OSL or the photoconductivity stimulation spectra and the measurement and analysis of both are presented in this chapter.

4.2 Photoconductivity

For a system with multiple traps the rate equation describing the traffic of charge into and out of the conduction band is

$$\frac{dn_c}{dt} = \phi(h\nu)\sum_i \sigma_i(h\nu)n_i - \sum_i c_i(N_i - n_i)n_c - c_{F^+}n_c N_{F^+} \tag{4.1}$$

where the summations are over all the trapping states. Here, $\phi(h\nu)$ is the flux incident on the sample at a particular stimulation energy $h\nu$. c_i is the capture cross-section multiplied by the free carrier thermal velocity and is known as the "capture rate". $\sigma_i(h\nu)$ is the photoionization cross-section[53] given by:

$$\sigma_i(h\nu) = \begin{pmatrix} a\frac{\sqrt{E_i}(h\nu - E_i)^{3/2}}{h\nu(h\nu+\gamma E_i)^2} & h\nu \geq E_i \\ 0 & h\nu < E_i \end{pmatrix} \tag{4.2}$$

where a is a scaling constant, E_i is the optical threshold energy for ionization from trap i, and γ is related to the charge carrier effective mass m^* by:

$$\gamma = 1 - \frac{m_0}{m^*}. \tag{4.3}$$

m_0 is the free rest mass of an electron. Under steady-state conditions, $dn_c/dt = 0$ and,

$$\phi(h\upsilon) \sum_i \sigma_i(h\upsilon) n_i = \sum_i c_i(N_i - n_i)n_c - c_{F^+} N_{F^+} n_c \tag{4.4}$$

Eq.(4.4) can be rearranged to solve for the photoionization cross-section, thus:

$$\sum_i \sigma_i(h\upsilon) = \frac{n_c}{\phi(h\upsilon)} \sum_i \frac{c_i(N_i - n_i) - c_{F^+} N_{F^+}}{n_i} \tag{4.5}$$

If Δn_i electrons are removed from trap i during the stimulation, then, under conditions of "weak stimulation" such that $n_i >> \Delta n_i$ we may assume that n_i and N_{F^+} are approximately constant. Under these conditions the summation on the right hand side is approximately constant and we can write:

$$\sum_i \sigma_i(h\upsilon) = \left(\frac{K}{\phi(h\upsilon)}\right) n_c \tag{4.6}$$

where K is a constant.

Using eq.(4.6) there are two ways to determine the photoionization cross-section. The first, originally proposed by Grimmeiss and Ledebo [54] consisted of varying the incident flux of light $\phi\,(h\nu)$ so as to maintain a constant photoconductivity (*i.e.* constant n_c) from the sample. Hence, the photoionization cross-section as a function of stimulation energy is then equal to the inverse of the required photon flux. The second method is to maintain a constant photon flux across the sample and measure the change in the photoconductivity as

a function of stimulation energy. In this case the photoionization cross-section is simply proportional to the change in photoconductivity (n_c) as a function of stimulation energy.

However, we are measuring the sum of the photoionization cross-sections of several traps at any given wavelength and thus, whereas at low energies only contributions from the shallowest traps my be observed, as the stimulation energy increases contributions from progressively deeper traps are included. Thus, by scanning over a broad stimulation spectrum, the number of trapping levels can be determined through fitting of the data to eq.(4.6), using curves of the form of eq.(4.2).

Similarly, with OSL one can relate the wavelength dependence of the OSL emission to the photoionization cross-section by considering recombination rate, thus:

$$I_{OSL} = \eta \frac{dn_{F^+}}{dt} = \eta c_{F^+} n_c N_{F^+} \tag{4.7}$$

where η is the luminescence efficiency. Again, if $n_{F^+} \approx$ constant, then the OSL intensity is directly proportional to n_c (*i.e.* the photoconductivity) and hence is dependent on $\sigma_i\,(h\nu)$ only.

4.3 Experimental Details

The Al_2O_3:C samples used were obtained from either Medus (Russia - so-called TLD 500 samples[4]) or Landauer Crystal Growth Facility (USA - formerly Stillwater Sciences LLC). The samples were circular single crystal chips of approximate dimensions 5mm in diameter x 1mm thick. The samples exhibited intense OSL and were typical of the Al_2O_3:C samples used in radiation dosimetry. An Oriel model 6333 halogen lamp and an

Oriel model 63163 deuterium lamp were used as illumination sources. The halogen lamp was used primarily for stimulating the sample at wavelengths greater than 300 nm while the deuterium lamp was used for stimulating at wavelengths less than 350 nm. A Spex model 1681 with a 1200 line/mm grating blazed at 280 nm and with a $\Delta\lambda$ of 0.3 nm/mm was used to select the appropriate wavelength. A series of long-pass filters was employed for light of wavelengths longer than 400 nm, while for light of wavelengths shorter than 400 nm a UG 5 bandpass filter was used in order to avoid complications arising from 2^{nd}-order effects.

For the photoconductivity measurements, palladium electrodes were deposited on the surface of the sample using vacuum deposition or sputtering. Fig.4.1 shows the transmission of palladium as well as several other metals tested. Palladium was ultimately selected because it had the flattest overal transmission spectra of the metals tried and was robust enough to resist scratches from the electrodes. In order to minimize surface currents, a grounded guard ring configuration was employed as was shown in fig2.6. One electrode was thin enough to allow light to pass through. Over the wavelength range used in the experiment palladium does not have a perfectly flat transmission spectrum, so a Varian Cary 5 spectrophotometer was used to measure the transmission of a thin film of the metal (the same thickness as that used for the electrode) evaporated onto a fused silica window. This spectrum was used to correct for wavelength-dependent transmission of the electrode.

The samples were first annealed at 1270 K for 10 minutes and cooled in air. They were then irradiated at room temperature using either a ^{60}Co gamma source at a dose rate of 9 $mGys^{-1}$, or a $^{90}Sr/^{90}Y$ beta source at a dose rate of 5.19 $mGys^{-1}$. A Keithley

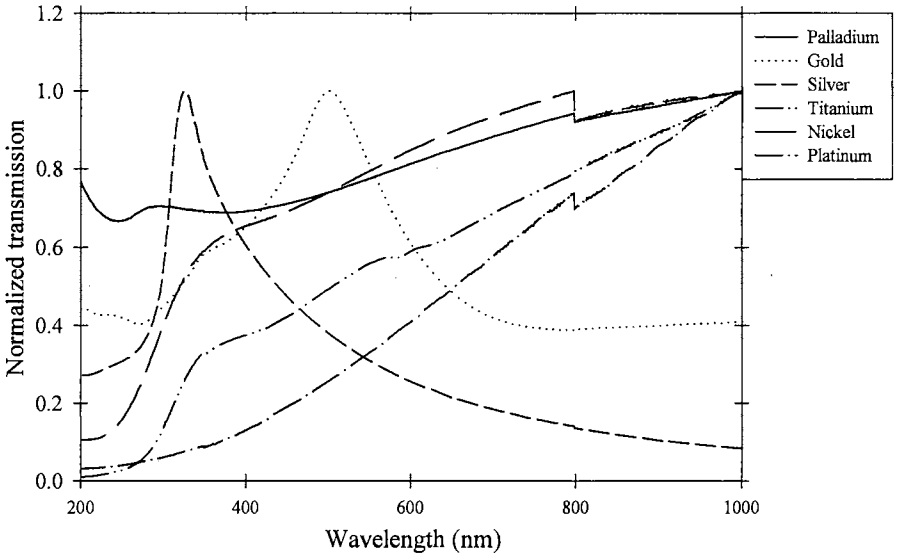

Figure 4.1 Normalized transmission of palladium, gold, silver, titanium, nickel, and platinum over the range 200-1000nm. The transmission was measured by evaporating a thing layer of metal onto a fused silica window. The transmission of the fused silca window over the wavelength range was accounted for.

model 617 electrometer was used to both supply the bias voltage (100 V) across the sample and to measure the photo-induced current. The sample was mounted in a holder with two gold probes serving as the electrical conduit to the electrometer. Care was taken to ensure that the guard ring was grounded with respect to the electrometer. Light of appropriate wavelength was focused onto the surface for 15 seconds to allow the charge in the conduction band to reach equilibrium. Current measurements were then made using 15 averages over a period of several seconds. The data were corrected to the spectral response of the lamp, *i.e.* the incident number of photons per unit area per unit time, and for the transmission of the front electrode. Depletion of charge from traps was less than 5% over a complete scan and thus the conditions of "weak stimulation", as required for the analysis, were assumed to be met.

For the OSL measurements, the same light sources, monochromator and cut-off filters were used. Two 420 nm interference filters with 10 nm FWHM were used to separate the stimulation light from the emission light. A Thorn-EMI model 9635QB bialkali PMT was used to detect the luminescence from the sample and the photons were counted using a Stanford Research Systems SR 420 multichannel scaler. The sample was stimulated at a particular energy for 1 second while the luminescence was counted before moving to the next stimulation energy. The amount of charge depletion during the course of the entire measurement was less than 5% and thus the conditions of "weak stimulation" were again considered to be met.

4.4 Analysis Methods

From recent works by Agersnap Larsen and colleagues[52], [55], it has been shown that the TSC and TL curve shapes are the result of a distribution (in energy) of populated traps. Thus, the present data were modelled using a Fredholm integral equation of first kind, of the form:

$$S(h\upsilon) = \int g(E)\sigma(h\upsilon, E)dE \tag{4.8}$$

where $S\,(h\nu)$ is the measured photoconductivity or OSL, and g is a weighting factor which defines that portion of the photoconductivity or OSL signal which is due to a particular trap, at a given stimulation energy $h\upsilon$. E is the threshold energy for optical ionization. Thus, $g(E)$ is the shape of the distribution (in threshold energy) of occupied traps. $S(h\upsilon)$ is measured and $\sigma(h\upsilon, E)$ is known from eq.(4.2). A non-negative least-squares (NNLS) technique [55] was used to solve for the unknown shape of the distribution $g(E)$.

The technique consists of minimizing

$$\eta^2_{\xi_i} = \sum_i^{ndata} \left(\frac{y_i - \sigma_{ij} g_i}{\xi_i} \right)^2 - \alpha \sum_i^{ndata} g_i^2 \qquad (g_i \geq 0) \tag{4.9}$$

where y_i represents the measured data, $\sigma_{ij} = \sigma(h\upsilon_i, E_j)$ is one of a set of fitting equations that model the photoionization cross-section, and ξ_i is the standard deviation in the data. The distribution parameter g_i scales the photoionization cross-section such that it matches the experimental data. Because this is an 'ill-conditioned' problem, an additional parameter α (Tikhonov's regularization parameter) helps to stabilize the solution.[55]

In order to take the data over a large stimulation energy range, different light sources and different filter combinations were used and the data were then "stitched" together to

form the complete spectrum. This, unfortunately, causes the standard deviation in the data to be different for each point and to be discontinuous. The solutions to eq.(4.9) are strongly attracted to the discontinuities. In order to satisfy the criteria that $\eta^2_{\xi_i}$ is small but no smaller than the noise in the data and $\boldsymbol{\xi}_i$ is continuous, the distribution was solved using a constant value of $\boldsymbol{\xi}$, thus:

$$\eta^2 = \frac{1}{\xi^2} \sum_i^{ndata} (y_i - \sigma_{ij} g_i)^2 - \alpha \sum_i^{ndata} g_i^2 \qquad (g_i \geq 0) \tag{4.10}$$

This distribution was then used in eq.[55] to test for an appropriate minimum.

4.5 Experimental Results and Discussion

4.5.1 bigskip TL/TSC

Examples of typical TL curves for some of the samples used in this study are shown in Fig.2.3. The data indicate an array of trapping states, becoming thermally unstable over the temperature range from 300 to 1023 K. It is difficult to assess the relative concentration of the states using TL, however, because of thermal quenching of the F-center luminescence (420 nm emission) [25]. As discussed in detail in chapter 3, an additional non-radiative recombination pathway to the F-center becomes available at higher temperatures. Since there is more than one recombination pathway, the amount of TL is no longer directly proportional to the amount of charge in the trap.

TSC, however, does not suffer from thermal quenching. TSC curves for the same three samples are shown in Fig.2.7 where we see that each sample possesses large concen-

trations of deep states. All of the samples show TSC peaks at ~600 K and in the region of ~900 K which are much more intense than the TSC peak in the ~450-500 K region, indicating that the amount of charge stored in deep traps is considerable larger than that stored in the ~450-500 K traps. Sample 76 also shows TSC signals near 700 K and 800 K. A comparison of these data with the TL curves in Fig.2.3 clearly shows the effect of thermal quenching at higher temperatures.

4.5.2 Photocurrent measurements

Figure 4.2 shows the photoconductivity and OSL intensity (at a fixed emission wavelength of 420 nm) as a function of stimulation wavelength. The photoconductivity was measured by two methods: I) Holding the incident photon flux constant at all wavelengths and measuring the subsequent photoconductivity, and II) holding the photoconductivity constant at all wavelengths and measuring the photon flux required to achieve this (the Grimmeiss-Ledebo method)[54]. One advantage of the Grimmeiss-Ledebo method is that the charge in the conduction band is known to be in steady-state whereas in the other method it is assumed to be steady state. However, since the curve shapes are similar between the two methods, we assume that charge in the conduction band is in steady state for both methods. Method I, however, is much easier and faster to do and all photoconductivity data shown from this point on were taken using this technique. Additionally, a comparison of the OSL stimulation spectrum is also shown in the figure. The OSL was obtained using a fixed emission wavelength of 420 nm. The shape of the OSL stimulation spectrum corresponds well with that of the photoconductivity spectra. The most noticeable feature with the OSL is the

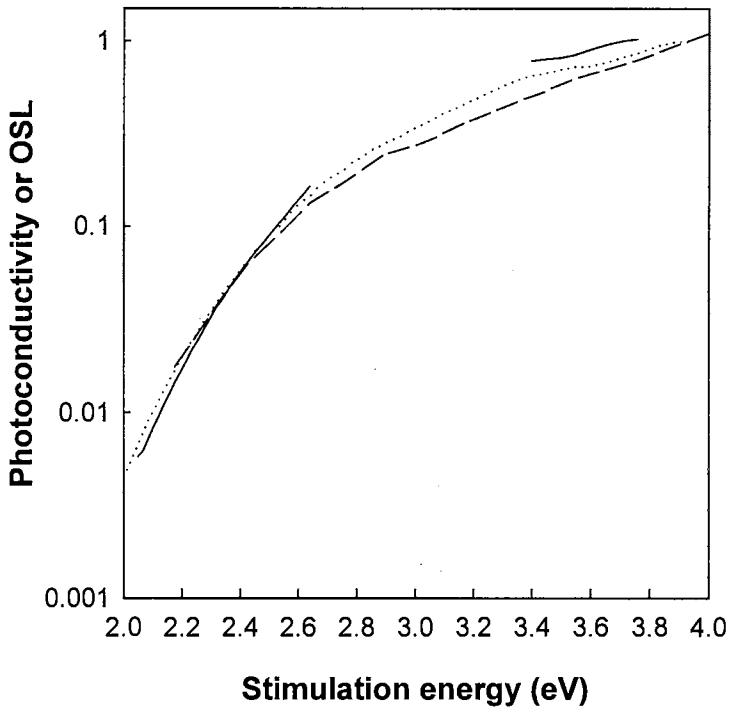

Figure 4.2 Comparison of (normalized) photoconductivity and OSL stimulation spectra for irradiated Al_2O_3:C (sample 76). The dose given in each case was 300 Gy from a ^{60}Co source. The photoconductivity data were taken using either the constant photon flux method (dotted line) or the constant photoconductivity method (*i.e.* the Grimmeis-Ledebo method[54] - dashed line). The OSL spectrum (full line) was obtained using a fixed emission wavelength of 420 nm. The data were all normalized to unity at a stimulation energy of 4.0 eV.

lack of data in the range 2.7-3.4 eV due to overlap between the emission light and stimulation light, making it difficult to obtain data over the entire spectral region. Since the shape of the OSL spectrum is similar to that of the photoconductivity, as expected, we believe that the analysis of, and the conclusions drawn from, the photoconductivity measurements are also valid for OSL.

Fig. 4.3 shows typical normalized photoconductivity spectra from a sample irradiated with various doses of gamma radiation. The stimulation range for these data is very wide,

extending from the infrared to the limit of the current range of measurements (at 4.1 eV), supporting the observation by Bulur *et al.*[37] of OSL emission following infrared stimulation. Over the range of gamma doses used (10 Gy - 1000 Gy) the shape of the spectra remain similar with the exception that the photoconductivity at higher stimulation energies (between 3.4 and 4.1 eV) increases more rapidly with dose that the data at lower stimulation energies. This suggests the preferential population of deep traps (with optical threshold energies near 3.8 eV) at high doses, in agreement with the observation of Agersnap Larsen *et al.* using TSC [52]. The overall shapes of these photoconductivity stimulation spectra are very similar to data taken by Akselrod *et al.*[57] using optically stimulated exoelectron emission.

Attempts were made to fit the data to two single functions of the form of eq.(4.2), leaving the shape parameter γ and the threshold ionization energy E_i as free parameters. However, the attempts were unsuccessful. While the flattened higher energy part of the data fit very nicely with the theoretical function, the curved lower energy part of the data was much too broad to fit. There are two possible reasons for this. The first is that we are observing thermal broadening of the absorption tail. The second possible explanation is that we are not looking at a single trap depth but a distribution of traps centered around E_i.

Attempts were made to take photoconductivity at 77 K in order to measure the effects of thermal broadening, but the signal-to-noise ratio was too high for any formal conclusions to be drawn. As discussed in the Introduction, however, there is existing evidence for a distribution of trap depths in this material. Walker *et al.*[34] studied the temperature

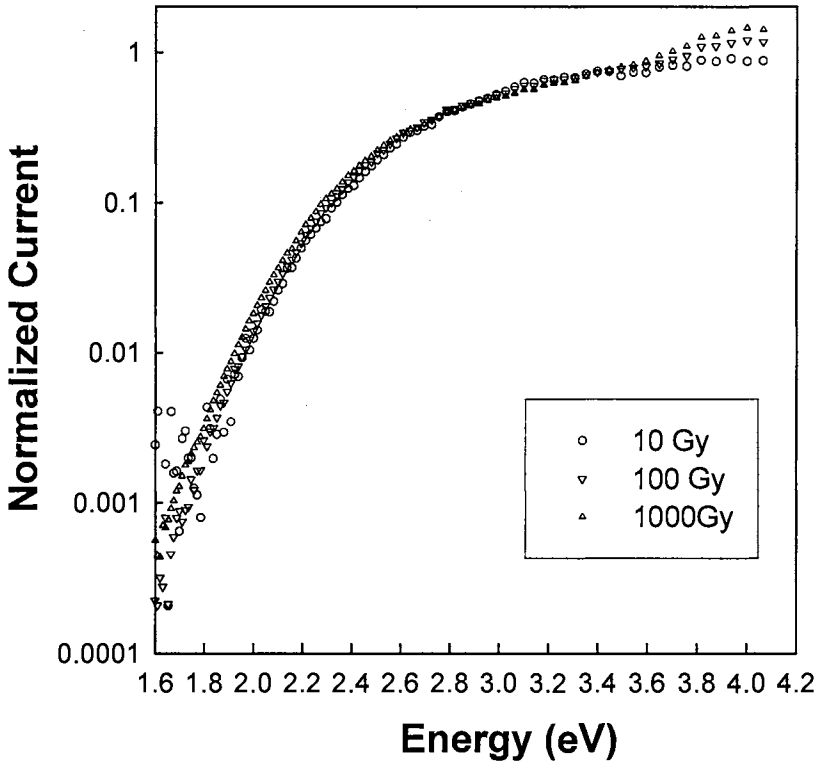

Figure 4.3 Normalized photoconductivity stimulation spectra as a function of absorbed dose for sample #170. The data were normalized at 2.8 eV.

dependence of the 450 K TL peak as a function of dose. They found that the abnormal dose dependence of the peak could not be explained with either simple 1^{st}-order or 2^{nd}-order kinetics using one trap. They concluded that the peak was actually a superposition of several 1^{st}-order TL peaks. Similarly, Agersnap Larsen *et al.* [52] made a detailed study of the shape of the TSC peaks in Al_2O_3:C. They also found that the TSC peaks could not be modelled using a single 1^{st}-order or 2^{nd}-order TSC peak. Using a NNLS technique similar to the one in this paper[55], they found the TSC peaks to be a superposition of several 1^{st}-order signals. Therefore, we feel that these reports of distributions of trapping states in the TL and TSC of Al_2O_3:C are justification for using a distribution of trapping states in the analysis of the present photoconductivity (and OSL) data.

The data were, therefore, deconvolved using the Fredholm equation (eq.(4.8)) and the NNLS technique as described above. In order to determine an acceptable effective mass, the data were first fit using a single function of the form of eq.(4.2). This gave an estimate for the shape parameter γ and thus the effective mass. The value obtained for γ was -0.92 which yields an effective mass of 0.523 m_0. This compares with the value of 0.35 m_0 obtained by Xu and Ching [59] using band structure calculations. Thus, the value for the shape parameter we obtained by using a single function was assumed to be a reasonable approximation, and was used in all further analyses of the data.

The energy distributions determined by the NNLS technique for the three different samples, and after several radiation doses, were determined and example results, for sample 76, are shown in Fig.4.4. An example of a fitted data set is shown in Fig.4.5. Although the analyses of the other samples showed considerable variation in detail, the most obvious and

consistent feature of the fits was that three distinct distributions were present: a low energy distribution between ~1.7 eV and ~2.5 eV, a second between ~3.0 eV and ~3.8 eV, and a third between ~3.8 eV and ~4.9 eV. This supports the conclusions of Agersnap Larsen *et al.*[52], from a similar analysis of TSC curves, who also find three distinct distributions of trapping levels. A direct comparison of the energy values cannot be made, however, due firstly to the expected differences in the optical and thermal trap depths, and secondly due to the fact that the analysis technique applied by Agersnap Larsen *et al.*[52] to the TSC data used only one attempt-to-escape frequency factor (effectively assuming the same capture cross-section for all the traps), which will inevitably skew the obtained thermal trap energies.

As the dose given the sample is increased, the distributions of traps determined from the deconvolution of the data changes. As the dose increases the distribution of the shallower traps becomes broader, especially at the lower energy side and deeper trapping states appear. This observation also agrees with the results of the analysis of the TSC data[52], and the dose dependence of the TL data[34]. Furthermore, the results indicate that the deepest trap has the highest number of available trapping states and the shallowest distribution has the least. This is again is consistent with published TSC data[52] and the shape of the TSC curves shown in Fig. 2.7.

4.5.3 Effects of thermal annealing

Fig. 4.6 shows the effects of annealing temperature on the photoconductivity spectra. Heating the samples to 473 K for 10 minutes and then cooling to room temperature for photo-

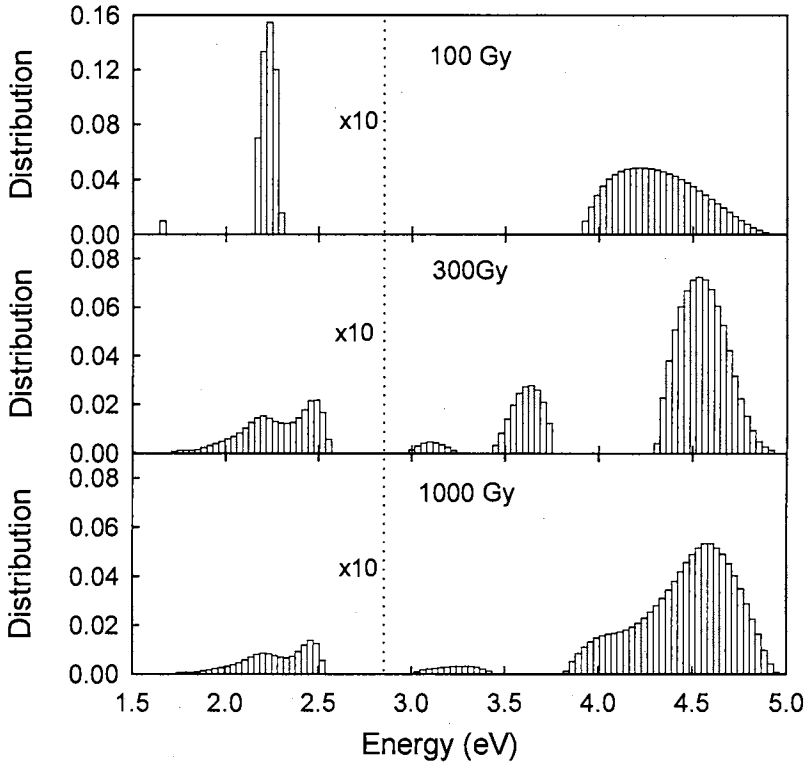

Figure 4.4 Optical threshold energy distributions for sample 76 obtained from a deconvolution of the photoconductivity stimulation spectra at three absorbed gamma doses, as indicated.

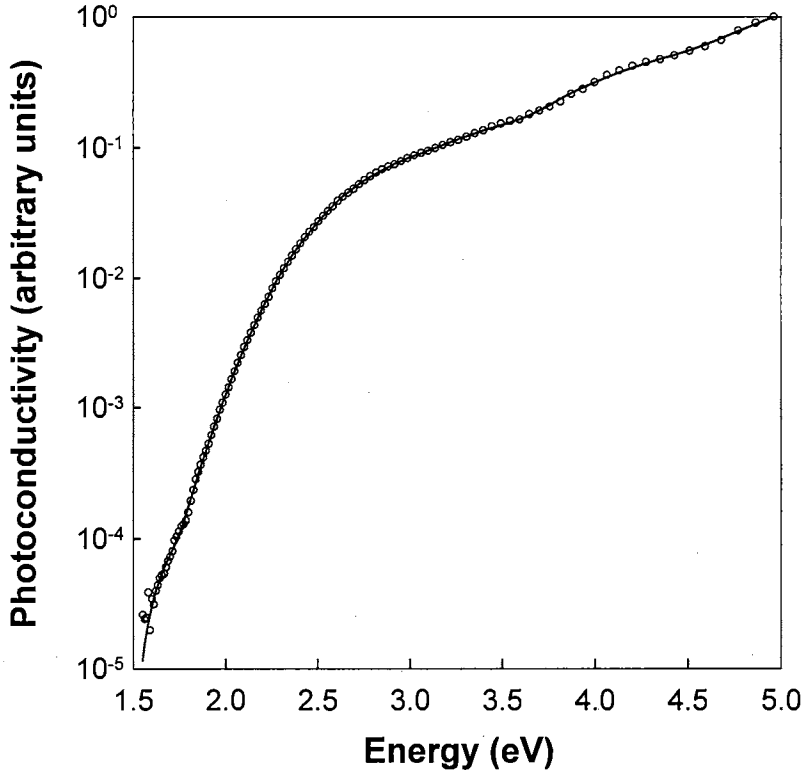

Figure 4.5 Comparison of the experimental data with the fit (using equations (4.2) and (4.8)) for sample 76 irradiated with 300 Gy of ^{60}Co gamma rays. The line represents the fit and the dots are the photoconductivity data.

conductivity measurement decreases the photoconductivity in the region of 1.5-3.5 eV - *i.e.* in the region of the shallowest traps. From Figs. 2.3 and 2.7 we observed that TL and TSC peaks are observed in this temperature region when heated at 1 Ks^{-1}, demonstrating that the traps responsible for these signals are thermally unstable in this temperature range. Thus, it is assumed that the charges stimulated into the conduction band with optical energies of 1.5 eV (or higher) are being excited out of the trap that gives rise to these TL and TSC peaks. After annealing the sample at 593 K for 10 minutes, the photoconductivity shows a further decrease at higher stimulation energies, such that photoconductivity is now observed only for stimulation energies greater than ~3.6 eV. Unfortunately, the conductivity at this point is very weak with a high signal-to-noise ratio. Fig. 4.7 shows an attempt at deconvolving the photoconductivity data in Fig. 4.6. As was expected, after a preheat to 473 K, the low energy distribution is completely gone, but the two deeper distributions remain. After annealing the sample at 593 K, the 3.5 eV traps contribute little to the distributions. (It should be noted that the latter data set only goes as low as 3.6 eV). The distribution at 4.5 eV shows a low energy shoulder (near 4.1 eV). This is believed to be an artificial peak arising because of the high signal-to-noise ratio.

To determine how much each of the traps contribute to the OSL signal we conducted an experiment in which the samples were irradiated, then pre-heated to a given temperature, cooled to room temperature, and the OSL signal measured at a given stimulation wavelength. Fig.4.8 shows the results of one such experiment in which the intensity of the OSL emission, at an emission wavelength of 420 nm and for a fixed stimulation wavelength of 465 nm, is plotted as a function of preheat temperature. In each case the sample was

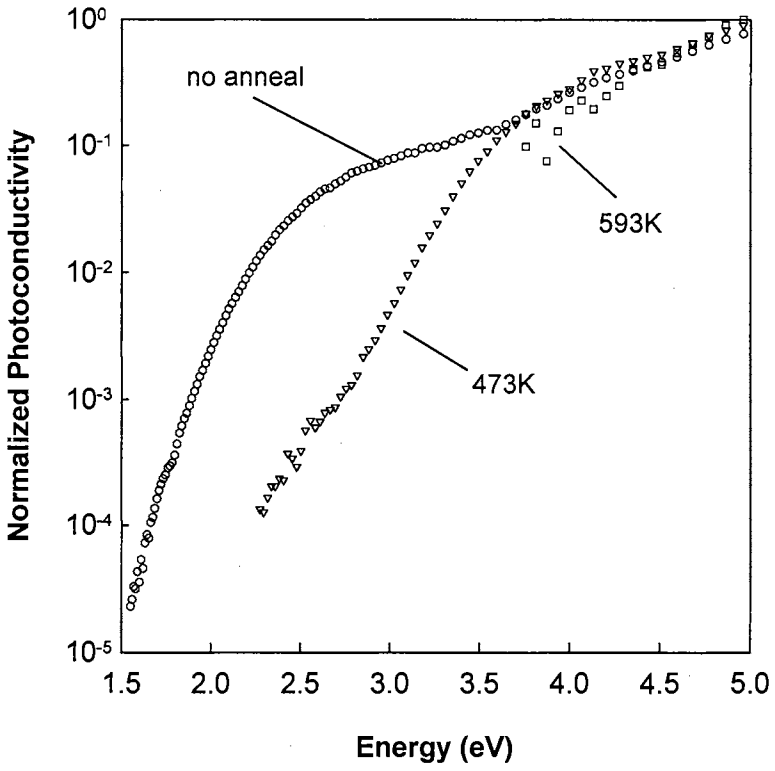

Figure 4.6 The effect of pre-annealing (for 10 minutes at each of the temperatures indicated) on the photoconductivity spectra. The sample is #76, and the dose given was 300 Gy of ^{60}Co gamma rays.

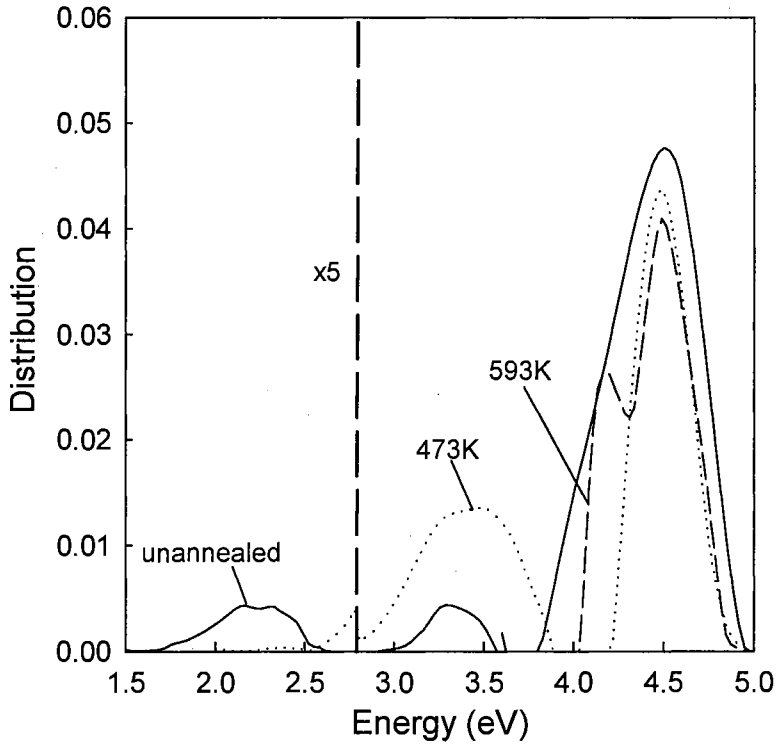

Figure 4.7 Optical threshold energy distributions for sample #76, after irradiation and annealing at each of the temperatures indicated for 10 minutes.

preheated to an increasingly elevated temperature at a rate of $1 Ks^{-1}$ before being cooled to room temperature and the OSL measurement taken. One can clearly see the presence of several steps in the data. Each step corresponds to the thermal emptying of trapping states which then no longer contribute to the OSL signal. The largest step is centered at $\sim$500 K and corresponds to the TL/TSC signal in this temperature range. As shown above, the traps corresponding to these signals give rise to photoconductivity with threshold energies distributed between $\sim$1.7 eV and $\sim$2.5 eV. At a wavelength of 465 nm (stimulation energy 2.6 eV) most (>90%) of the observed OSL (and photoconductivity) originates from these traps. A second step is observed at $\sim$ 600 K and this corresponds to the trap distribution from $\sim$3.0 eV and $\sim$3.8 eV. At this 465 nm, this signal comprises <10% of the OSL (and photoconductivity) signal. A stimulation energy of 2.6 eV is insufficient to stimulate charge from deeper traps. As a result very little change in the OSL output is observed at higher annealing temperatures, corresponding to deeper traps. The largest change is observed for sample TC4, for which a reduction in OSL of only a few tenths of a percent is observed as the temperature increases to over 900 K. For higher stimulation energies, however, the deep traps contribute more to the OSL. For a stimulation energy of 4.6 eV (270 nm) we observed that about 10% of the OSL signal originates from the deeper traps for an absorbed dose of 300 Gy.

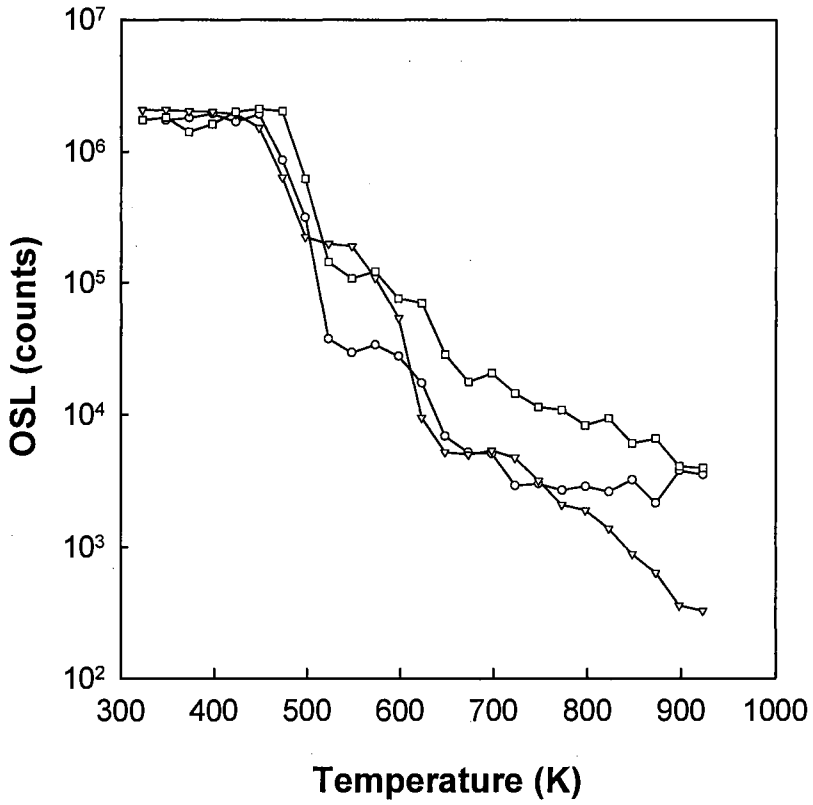

Figure 4.8 The intensity of the OSL emission (emission wavelength 420 nm and stimulated at 465 nm) as a function of preheat temperature, for three different samples. The samples were cooled to room temperature after each annealing step to make the OSL measurement and each measurement was the integrated OSL emission for a stimulation time of 10 seconds. The samples were each irradiated with 300 Gy from a $^{90}Sr/^{90}Y$ beta source

4.6 Further Discussion

The purpose of this work was to determine, and analyze, the optical stimulation spectra for photoconductivity and OSL from radiation dosimetry-quality Al_2O_3:C. By maintaining the stimulation photon flux constant under conditions of weak stimulation, the obtained photoconductivity-versus-wavelength spectra yield directly the dependence of the photoionization cross-section as a function of wavelength. The obtained spectra indicate photoionization from radiation-induced traps over a wide range of optical stimulation energies, from the infra-red to the limit of the stimulation energy range used in the current measurements (at 4.9 eV). At each of these stimulation wavelengths emission from excited F centers (peak emission at 420 nm) is also observed and we have shown that the photoconductivity and OSL stimulation spectra are essentially the same. This indicates that Al_2O_3:C is a viable radiation dosimeter using OSL and lends itself radiation dose measurement using a wide range of stimulation light sources. This fact, in turn, suggests that there is a wide array of trapping states which contributes to the OSL and photoconductivity signals in irradiated Al_2O_3:C. An important finding is that the stimulation spectra cannot be explained using discrete values for the trapping energies of these states. Instead, the analysis indicates that several distributions of states must be present, with optical threshold energies from as low as $\sim$1.7 eV to as high as $\sim$4.9 eV. It is this distribution of contributing localized states that give rise to the very wide range of stimulation energies observed for this material.

Although the current data are insufficiently noise free to be confident about the detailed shape of the obtained distributions, the assertion that the trapping states are distributed in energy supports earlier conclusions arising from studies of TSC and TL in which the dose dependence of the TL and TSC curves could be explained only on the basis of a distribution of thermal traps depths.[52],[34] The dose dependence of the present data also supports these earlier studies. The step annealing measurements show that the TL and TSC signal near 400-500 K is caused by the same localized trapping states which give rise to OSL and photoconductivity for stimulation energies below ~2.5 eV. The traps related to these signals are distributed in energy from ~1.7 eV and ~2.5 eV and this distribution is dose dependent, such that it widens to lower energies as the dose increases. This clearly supports the TL [34] and TSC[52] results which demonstrated that the TL and TSC peaks shift to lower temperatures as a function of dose. The TSC data also suggest that deep traps (*i.e.* corresponding to TSC peaks >600 K) become relatively stronger as the dose increases. This too is observed in the analysis of the photoconductivity spectra observed in this study.

Most applications of OSL in radiation dosimetry use stimulation light sources near the green region of the spectrum.[35], [36],[56] The step annealing measurements reported here suggest that at these stimulation wavelengths most (>90%) of the OSL stems from photoionization of the low energy (~1.7 eV and ~2.5 eV) distribution of traps - especially at the low doses generally of interest in personal or environmental radiation dosimetry. At higher stimulation energies, however, an increased contribution from the deeper traps is

observed, especially at high doses. These signals may prove to be of use in high dose dosimetry applications (sterilization, food processing, materials testing, *etc.*)

The current analysis used the same value for the effective mass throughout the stimulation range. *I.e.* the implicit assumption is that the photoionized charge carriers are all electrons. Studies of the effects of thermal annealing on the intensities of the F and F^+ center optical absorption bands after irradiation[36] indicate that the traps causing the TL/TSC peaks around 400 - 500 K, and, therefore, the traps in the optical stimulation range from $\sim$1.7 eV to $\sim$2.5 eV are indeed electron traps. The high temperature TL/TSC signals around 900 K, however, were shown to be caused by hole traps, in agreement with earlier studies by Akselrod and Goreleva[60]. Since the latter TL/TSC signals are caused by very deep traps, which are not contributing to the OSL or photoconductivity signals observed in the present work, we believe the assumption of electrons being the photoionized carriers over the stimulation wavelength range used in the present measurements is justified.

Chapter 5
r-OSL AND r-PC

5.1 Introduction

Conventional OSL and PC measurements are usually performed using a constant intensity illumination beam to excite the trapped charge carriers out of the traps. These methods were discussed in sections 2.3 and 2.4. If the charge recombination obeys a first-order process, then a simple exponential decay of the measured OSL or PC is expected. These experimental decay curves can often be accurately represented by several exponential curves as in figure 2.9, implying a superposition of several first order processes. This is generally a good approximation to the OSL or PC measured in Al_2O_3. However, retrapping processes, interactions between multiple traps and multiple recombination centers can all cause the decay measured under constant illumination to deviate from an expected first-order decay.[27],[49]

If one does not know the kinetic order of the retrapping process or the number of contributing components, then the decay of the OSL or PC under CW emission is easily misinterpreted. It is difficult to determine if the measured decay is the superposition of several first-order processes, as was shown in fig.2.9, or if it results from contributions from a 2nd or higher-order trapping center. In general, it is often difficult to know the exact number of traps which are contributing charge to the OSL or PC when under constant

illumination. Often, one finds that either the photoionization cross sections of different trapping centers are of similar magnitude such that the different decay processes cannot be easily resolved, or that so many contributing states exist such that it is difficult to know the precise number. In cases such as these, the decay of the OSL or PC is often modelled by assuming first-order kinetics and using the minimum number of decaying exponentials needed to accurately represent the data. Unfortunately, a major criterion for selecting the number of traps to model is how arbitrarily accurate one wants to fit the data.

For example, fig.2.9 was fit with 3 decaying exponentials. This was done in part because the previous chapter suggests that there are three different trapping distributions contributing to the OSL and PC, but it was also chosen in part because three exponentials were needed to give a 'good' fit to the data. All indications suggest that the charge trapping kinetics in Al_2O_3 are first order, but without this knowledge and the trap depth information gleaned from the previous chapter, one might have approached the fit of the OSL in fig.2.9 differently. Another number of decaying exponentials could be tried, or perhaps a 2nd (or higher) order OSL decay function could be used in order to fit the data. An additional complication is the energy distributions of the trapping centers themselves. As was discussed in Ch.4, the trapping centers are not found at discrete optical depths, but vary over a range of energies. These variations were attributed to groups of traps centered around an average optical depth as well as thermal broadening of the optical depths of these trap clusters. Given this rather complex trapping system in Al_2O_3, three decaying first-order exponentials are usually not sufficient to fit the OSL or PC decay.

An alternative measurement procedure for OSL has been proposed by Bulur [61] which does not use constant power illumination. Instead of maintaining the stimulation light at a constant intensity, the stimulation light is linearly increased according to the function $\phi[t] = \frac{d\phi}{dt}t$. Since the light ramp is being increased linearly, we can write $\frac{d\phi}{dt} = const = \gamma$, where γ is the ramp rate. In a measurement of this type, so-called rOSL, the luminescence will increase linearly until the traps begin to be depleted, at which point the signal drops off and eventually decays to zero. The time at which the luminescence peaks is dependent on the ramp rate γ and the photoionization cross-section $\sigma[\lambda]$ of the traps being being depleted. Multiple trap contributions to the OSL will result in multiple peaks in the rOSL. By appropriate choice of wavelength, the resulting ratios of photoionization cross sections between all the contributing traps can be varied such that different contributions to the OSL can often be resolved. This allows one to determine the number of states contributing to the OSL more easily than in CW-OSL.

In Al_2O_3:C, electrons liberated from electron traps are excited into the conduction band before they recombine with the luminescence center. From eq (2.15), the PC was shown to be proportional to the OSL. It should then be expected that linearly ramping the stimulation light of photoconductivity (rPC) will gives results very similar to rOSL.

5.2 Theory

5.2.1 First-order kinetics

Using a linearly increasing light ramp of $\phi[t] = \frac{d\phi}{dt}t = \gamma t$ and assuming a first-order process, then the change in the number of electrons in the conduction band is:

$$\frac{dn_c}{dt} = -\frac{dn}{dt} = c[t, h\nu]n \tag{5.1}$$

Recalling that $c[t, h\nu] = \phi[t]\sigma[h\nu] = \gamma t\sigma$, then the solution to (5.1) is:

$$n_c = N_0\gamma\sigma t \exp\{-\frac{\gamma\sigma[h\nu]t^2}{2}\} \tag{5.2}$$

where N_0 is the initial concentration of charge trapped in the trapping center.

Recalling eq. (2.12) and (2.14), the ramped OSL (rOSL) and ramped photoconductivity (rPC) can be expressed as:

$$I_{rOSL}[t, h\nu] = k_{OSL}N_o\gamma\sigma[h\nu]t \exp\{-\frac{\gamma\sigma[h\nu]t^2}{2}\} \tag{5.3}$$

$$I_{rPC}[t, h\nu] = k_{PC}e\mu V N_o\gamma\sigma[h\nu]t \exp\{-\frac{\gamma\sigma[h\nu]t^2}{2}\} \tag{5.4}$$

where $\frac{1}{\tau}$ in eq.(2.12) has been replaced with $\phi[t]\sigma[h\nu]$. If V and μ are constant, then

$$I_{rPC}[t, h\nu] = \frac{k_{PC}}{k_{OSL}}e\mu V(I_{rOSL}[t, h\nu]) \tag{5.5}$$

which is the equivalent of eq.(2.15). If there is more than one trap contributing to the OSL or the PC, then equations (5.3)-(5.4) simply sum the contributions of all components over the number of contributing states i:

$$I_{rOSL}[t, h\nu] = k_{osl}\sum_i N_i\gamma\sigma_i[h\nu]t \exp\{-\frac{\gamma\sigma_i[h\nu]t^2}{2}\} \tag{5.6}$$

$$I_{rPC}[t, h\nu] = k_{pc}\sum_i e\mu V N_i\gamma\sigma_i[h\nu]t \exp\{-\frac{\gamma\sigma_i[h\nu]t^2}{2}\} \tag{5.7}$$

This is the superposition principle and required first order kinetics.

5.2.2 General-order kinetics

The general-order kinetic model takes into account the probability of retrapping an electron before it has a chance to recombine with the recombination center. In the general-order kinetic model, eq.(5.1) is no longer true. For a general-order case, the change in the trapped electron concentration is:

$$\frac{dn}{dt} = c[t, h\nu]n^{\beta} \tag{5.8}$$

where $\beta = 2, 3, ..., n$. If we use a linearly increasing stimulation, then:

$$\frac{dn}{dt} = \gamma\sigma[h\nu]tn^{\beta}. \tag{5.9}$$

Solving for n[t]:

$$n = N_o(1 + \frac{\gamma\sigma t^2}{2})^{\frac{1}{1-\beta}}. \tag{5.10}$$

Recalling that the $I_{OSL} = -\frac{dn}{dt}$, then the rOSL becomes:

$$I_{rOSL}[t, h\nu] = k_{osl}N_0\gamma\sigma[h\nu]((\beta - 1)\frac{\gamma\sigma[h\nu]t^2}{2} + 1)^{\frac{\beta}{1-\beta}} \tag{5.11}$$

and the general order rPC becomes

$$I_{pc}[t, h\nu] = \frac{k_{pc}}{k_{OSL}}e\mu V(I_{rOSL}[t, h\nu]) = k_{pc}e\mu VN_0\gamma\sigma[h\nu]((\beta - 1)\frac{\gamma\sigma[h\nu]t^2}{2} + 1)^{\frac{\beta}{1-\beta}}. \tag{5.12}$$

An expression of the form of eqs.(5.6)-(5.7) for the general order rPC/rOSL cannot be obtained since first order kinetics are necessary for the superposition principle.

Integration of the rOSL or rPC model over all times results in a constant proportional to N_0, i.e. the area under the rOSL or rPC curves is a constant independent of ramp rate γ.

Because the rOSL and rPC are expected to give similar results, only rPC results will be discussed in the next few sections unless noted. As long as the applied bias, mobility,

luminescence efficiency and recombination lifetime in eq. (5.5) remain constant, this is true. In chapter 2, it was noted, however, that the effective potential was not constant in photoconductivity because of static charge buildup, but for the moment that will not be considered.

5.2.3 Single trapping center results

Figure 5.1 shows plots of first-order (solid line), second-order (dotted line) and third-order (dashed line) rPC model using a single trap with a photoionization cross-section of 0.001 with $\mu = 1, V = 1, \gamma = 1$ and N_0 =1. It can be seen that the different kinetic trapping order will produce slightly different curve shapes. The higher the order, the faster the rOSL/rPC will peak and the slower it will decay to zero. Because the area of the curves is proportional to N_0, this means also that the higher the order, the lower the absolute maximum of the rPC peak. Increasing the ramp rate γ causes the curve to peak at an earlier time as can be seen in fig.5.2 where ramp rates of $\gamma = 0.025, 0.5, 1, 2, 3,$ and 4 were used. Taking the time derivative of Eq.(5.4) and (5.12) and setting it to zero to find the time at which the rPC peaks, t_{max}, results in results in:

$$t_{\max} = \sqrt{\frac{1}{\gamma\sigma[hv]}} \qquad \text{First-Order} \tag{5.13}$$

$$t_{\max} = \sqrt{\frac{2}{\gamma(\beta+1)\sigma[hv]}} \qquad \text{General-Order} \tag{5.14}$$

Note that the general order $t_{\max}$ and the first order $t_{\max}$ differ only by the factor $\sqrt{\frac{2}{\beta+1}}$.

One of the advantages has been that has been attributed to these types of measurements is that the kinetic order of the OSL or PC can easily be determined simply by the

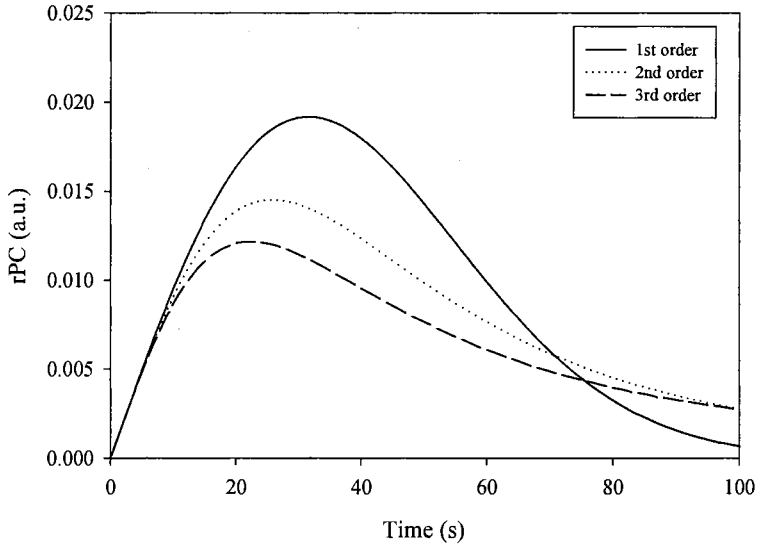

Figure 5.1 Simulations of a first order (solid), second order (dotted) and third order (dashed) rOSL or rPC curve using values of $N_0 = 1$, $\mu = 1, V = 1, \gamma = 1$, and $\sigma = 0.001$.

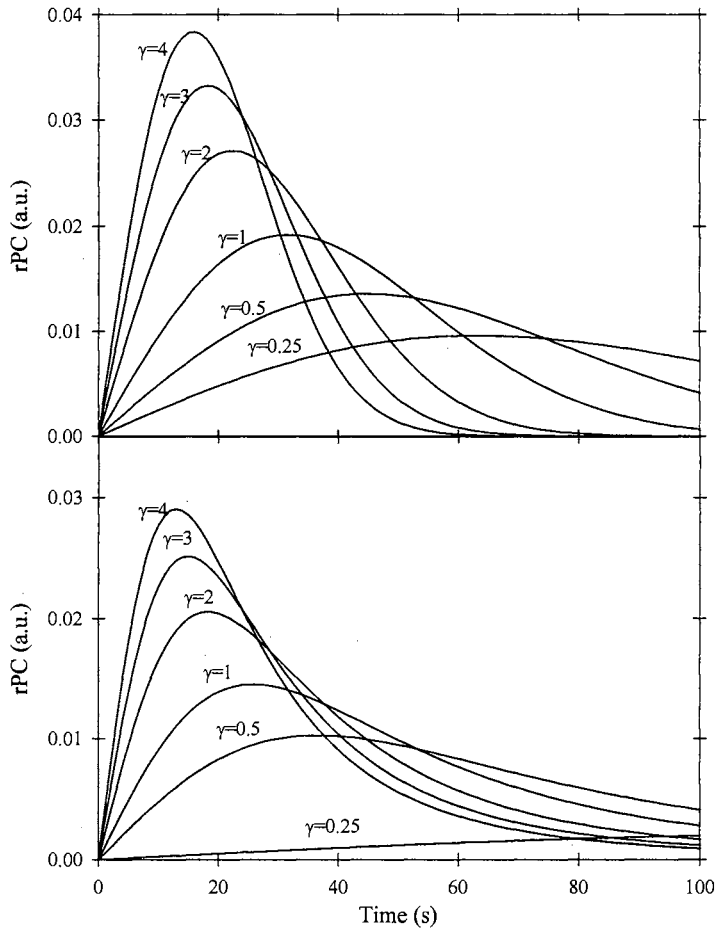

Figure 5.2 Simulated rOSL/rPC curves for different ramping rates. The upper figure is the results of first-order kinetics and the lower figure is results of second-order kinetics. Ramping rates of 0.25, 0.5, 1, 2, 3, and 4 were used in both.

shape of the rOSL or rPC curve.[61] Indeed, this is true in the simple case of a single trapping center as was illustrated in fig.5.1. Unfortunately, in the case of multiple contributions from different trapping centers, this is not true.

5.2.4 Multiple trapping center results

In the case of a single trapping center, knowledge of the energy dependence of the photoionization cross-section, $\sigma[hv]$, is not very important. As long as the ramp rate γ is known, then the value of $\sigma[hv]$ obtained at a particular stimulation can easily be determined using t_{max} and eq.(5.13) or eq.(5.14) depending on the order of the kinetics.

In the case of multiple contributing trapping centers, the energy dependence of $\sigma[hv]$ and the number of contributing trapping centers becomes of critical importance in order to correctly interpret the data obtained at a particular stimulation energy. At some wavelengths, a single rPC measurement can return more easily interpreted data than that of the corresponding PC measurement taken at a constant stimulation power. For example, fig.5.3 shows a simulated rPC measurent with two first-order contributions to the rPC. The photoionization cross-section of these two centers are 0.01 and 0.0001, respectively. In this case, the two different contributions to the rPC are easily resolved because each forms an independent peak. Since the peaks are so well resolved, fittings could be done in order to determine the kinetic order,and each t_{max} could be used to find the photoionization cross-section. This ideal case illustrates the utility of these measurement methods and how much useful information it is possible to glean from them. However, there are many cases where

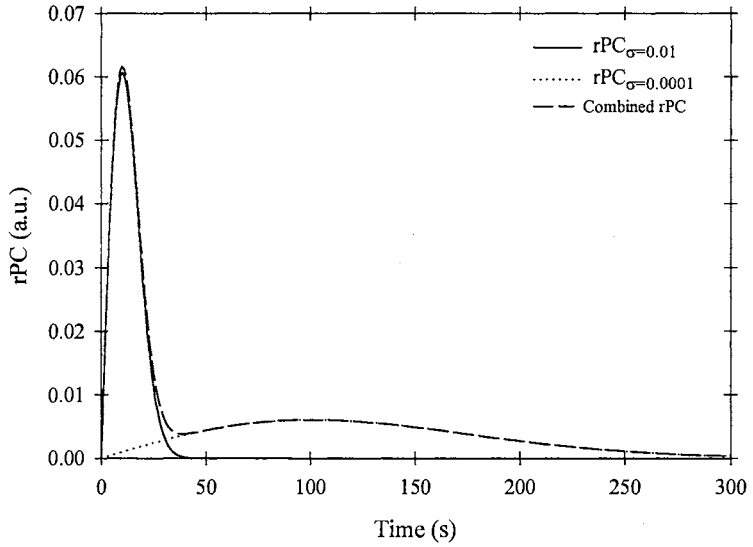

Figure 5.3 If the ratio of photoionization cross-sections is large enough, multiple distinct peaks can be seen. In this case, there are two first order contributions to the PC with $\sigma = 0.01$ (solid line) and $\sigma = 0.0001$ (dotted line). The combined rPC is shown as the dashed line.

the ratio of photoionization cross-sections are not sufficiently different such that multiple contributions to the PC are not easily resolved into independent peaks.

To illustrate this fact, let us assume that we have a sample with three discrete first-order trapping centers with threshold optical depths of 1.9eV, 2.5 eV and 2.9 eV. Furthermore, assume that the charge traps are electron traps and that the electron has an effective mass of 0.5 m, where m is the electron rest mass. With this information, the wavelength dependence of $\sigma[h\nu]$ can be generated and is shown in fig.5.4. Here, the shape of the resulting rPC varies with the stimulation energy. Fig. 5.5 shows a 3-D plot of the rPC over the stimulation range of 1.9-3.2 eV and the time range of 0-1500 seconds. For stimulation energies less than 2.5 eV, only contributions from the trapping center at depth of 1.9 eV appear and hence only one peak is seen. For stimulation energies between the ranges

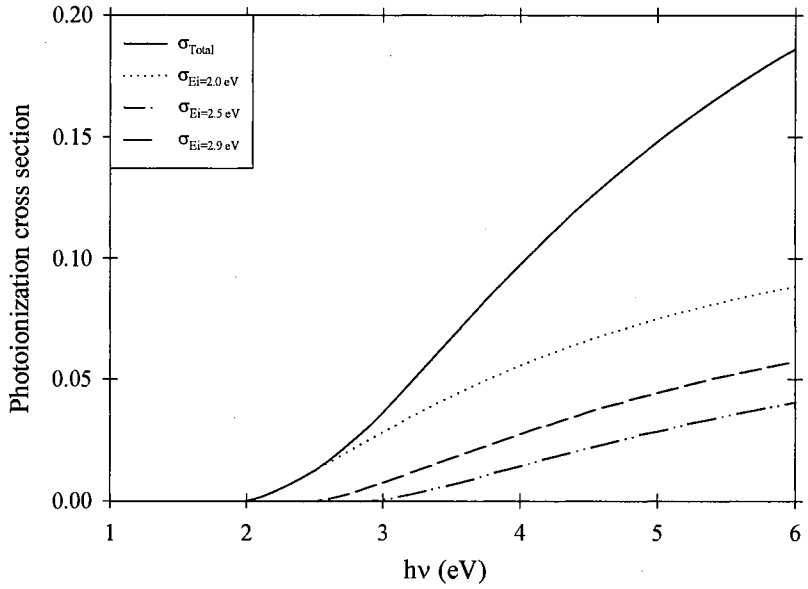

Figure 5.4 Energy dependence of the photoionization cross sections of discrete traps with optical threshhold energies of 1.9 ev, 2.5 eV and 2.9 eV as well as the total resulting photoionization cross section of all of them together.

of 2.5 eV and 2.9 eV, the rPC is a sum of contributions from both the 1.9 eV trap and the 2.5 eV trap. Over these stimulation energies, two distinct rPC peaks can be seen. The contribution from the 1.9 eV trapping centers peaks relatively quickly and decays to below that of the 2.5 eV contribution. The 2.5 eV contribution can be easily distinguished as a separate peak because most of its contribution occurs at a different time than the 1.9 eV rPC. There is almost no effect on the rPC from the deepest trapping state of 2.9 eV. As the stimulation energy reaches the range of this deepest trapping center, the 1.9 eV and 2.5 eV rPC peaks have merged to form one indistinguishable peak. The contribution from the 2.9 eV trap can be seen as an additional peak which reaches its maximum at a later time. As the stimulation energy increases, all three rPC peaks merge together to form one combined peak.

When the stimulation energy is such that the individual contributions of several first order rPCs merge to form one indistinguishable rPC peak, the kinetics of this combined peak do not look like first order. Fig.5.6 clearly shows that when stimulating this simulated sample at 3.2 eV, the resulting combined rPC looks identical to a second order rPC function which assumes only one trapping state at 1.9 eV. Depending on the optical depths and relative concentrations of the multiple traps in the sample as well as the stimulation energy, the resulting rPC not only can look as if it is a 2nd order process, but can also look like even higher orders as well (e.g. 3rd, 4th, etc.). Contrary to Bulur's suggestion[61], the kinetic order of the OSL or PC cannot be obtained from a single measurement at one stimulation energy without *a priori* knowledge of the number of trapping states or the energy dependence of the photoionization cross-sections.

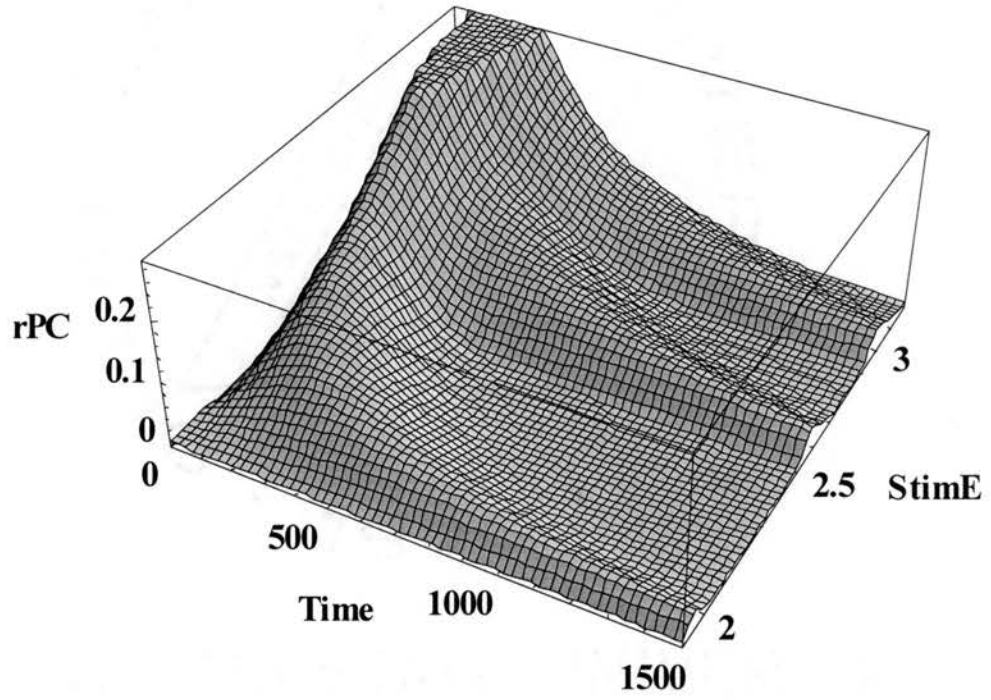

Figure 5.5 Simulation of the dependence of the rPC on the stimulation energy in a sample with discrete trapping centers at 1.9 eV, 2.5 eV, and 2.9 eV.

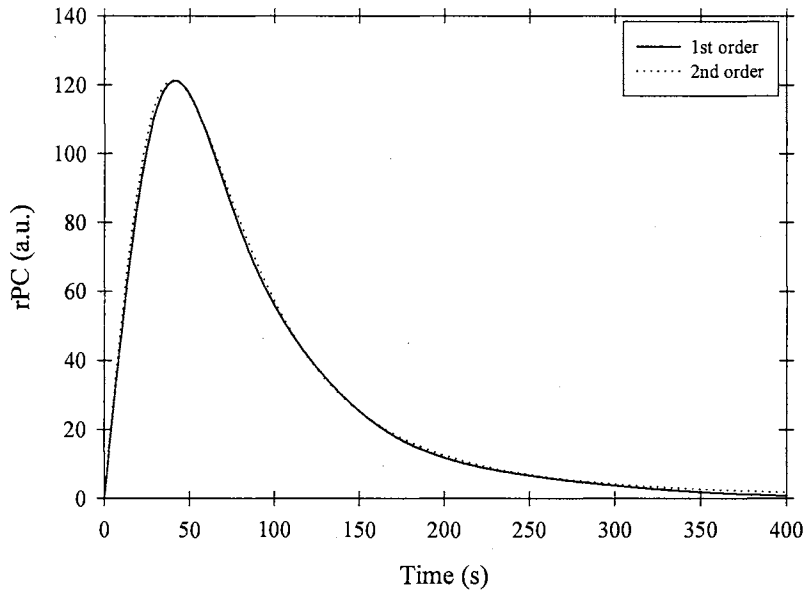

Figure 5.6 The solid line shows what the rPC would look like when stimulating a sample with first-order trapping centers at 1.9 eV, 2.5 eV and 2.9 eV with 3.2 eV light. The dotted line shows what the rPC would look like when stimulating a second order trapping center at 1.9 eV with 3.2 eV light.

While little information about the number of trapping states and the kinetic order can be obtained from a single rPC measurement, especially in the case of multiple trapping components that combine to give one single rPC curve, considerably more information can be obtained by taking rPC measurements at different stimulation energies and then comparing all the data. Fig.5.7 shows the shape of the three component first-order rPC and a single component second-order rPC changing with stimulation energy. If the measured rPC is a summation of several first order contribution, the change in the shape of the peak is different from that of an rPC which is only a single contribution from higher order kinetics. In this simulation, the sum of three first-order rPC peaks overlaps with one second order at a stimulation energy of $h\nu_s = 3.2$ eV. When using a stimulation energy of $h\nu_s = 2.8$ eV, the shoulder of the 2.5 eV trapping center is clearly seen and the contribution from the 2.9 eV trapping center is so small it contributes little. The shape of the first-order peaks is clearly different from the second-order peaks. If a stimulation energy of $h\nu_s = 4.0$ eV is used instead, the rPC that consists of 3 first-order components decays much faster than the single second-order rPC curve. In either case, the overlap of the two different rPCs occurs at just one stimulation energy.

To get a good fit of the data to all of the various stimulation wavelengths, not only must the kinetic order of the traps be chosen correctly, but also the correct number of trapping states must be used as well. If either of these two criteria are not fulfilled, the fitting of the model to the data will not give good results for all of the stimulation energies. Finding one set of energy states and kinetic orders that will fit the various rPC data taken at

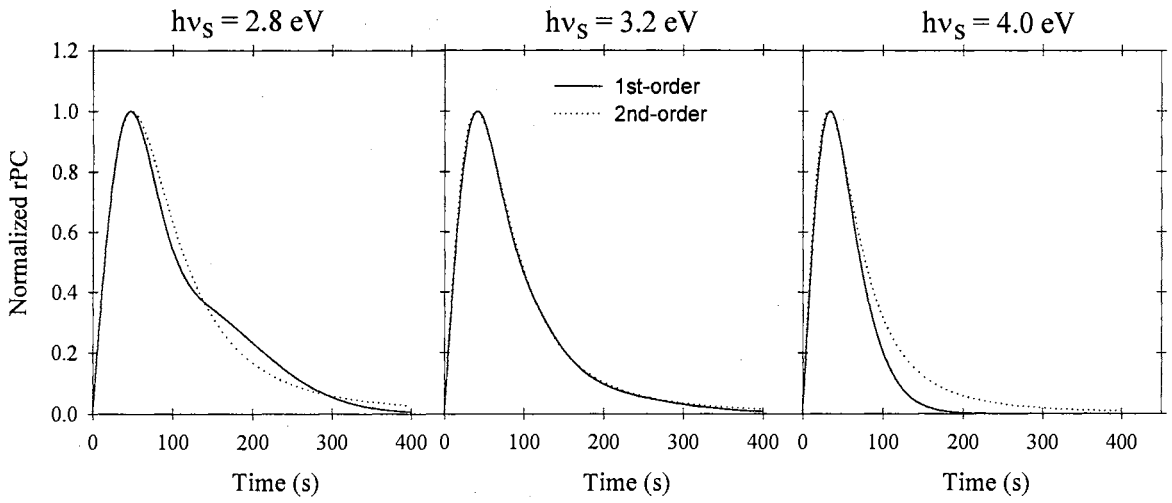

Figure 5.7 Simulation of the stimulation energy dependance of a combined first-order rPC and a second-order rPC.

different stimulation energies allows for certainty that the threshold energies and the kinetic order are correct.

Another difference found between a rPC consisting of a single contribution and that of an rPC consisting of multiple components is that the stimulation energy dependence of $t_{\max}$ is different. In a multi-component system, eqs.(5.13) and (5.14) no longer hold. A more general expression of

$$t_{\max}^2 - \sqrt{\frac{\sum_i \sigma[h\nu]_i \exp\{-\frac{\gamma\sigma_i[h\nu]t_{\max}^2}{2}\}}{\gamma \sum_i \sigma[h\nu]_i^2 \exp\{-\frac{\gamma\sigma_i[h\nu]t_{\max}^2}{2}\}}} = 0 \qquad (5.15)$$

must be solved to find the t_{max} of a rPC curve consisting of i first-order contributions. Eq.(5.15) can not be solved for t in an algebraic fashion. Fig.5.8 shows the numerical solution to eq. (5.15) over the stimulation range of 2.8 eV - 6.0 eV. Also shown is a plot of $t_{\max}$ for a single second-order rPC using eq.(5.14) with $\beta = 2$ for comparison. Clearly, the stimulation energy dependence of $t_{\max}$ is different between the summation of several first-order rPC components and a single second-order rPC component. Unfortunately, to correctly interpret the meaning of this stimulation energy dependence of $t_{\max}$, knowledge of $\sigma[h\nu]$ is necessary over the wavelength region used. Additionally, for a system with multiple contributions to the rPC, the stimulation energy dependence of $t_{\max}$ makes sense only with stimulation at or greater than the optical depth of the deepest trapping center. For stimulation energies considerably lower than this, multiple rPC peaks will be distinctly seen resulting in more than one $t_{\max}$.

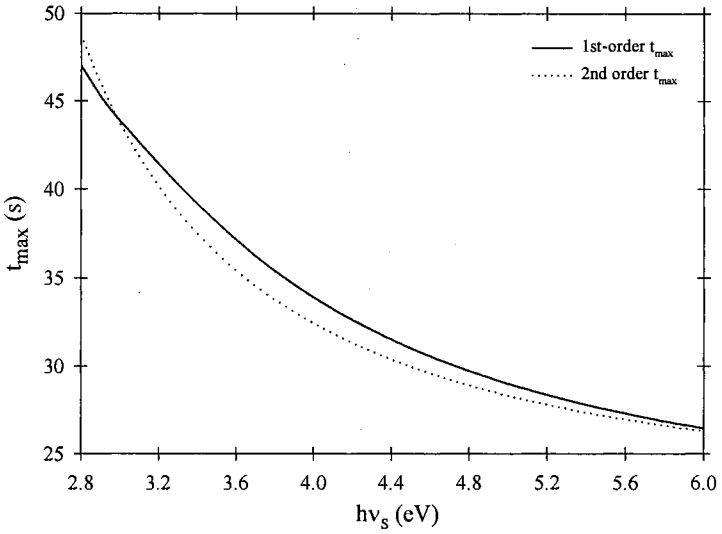

Figure 5.8 Stimulation energy dependence of t_{max} for an rPC consisting of three first-order contributions and for an rPC consisting of a single second-order contribution.

5.3 Experimental Setup

The samples used in this experiment were obtained from Landauer Inc. (USA) or Medus (Russia). They were approximately 5mm in diameter x 1 mm thick. They were first annealed at 1173 K for 10 minutes before usage. In order to measure photoconductivity, palladium electrodes were vacuum deposited onto the surface of the same in a typical guard ring fashion.

The light source used was a Spectra-Physics model 2020 argon-ion laser. The stimulation light was attenuated by using two circular graded neutral density filters from Coherent giving a total attentuation of OD5. These neutral density filters were mounted onto steeper motors controlled by a nuLogic nuDrive stepper motor controller. A 1/1000 cube beam sampler was used to direct a small percentage of the stimulation light onto a Newport 819UV detector interfaced to a Newport model 1830C power meter. Care was taken not to saturate the detector by using additional optical density filters to further attentuate the sampled beam.

A Keithley model 6127 multimeter was used to supply the bias voltage of 100V across the sample and to monitor the photoconductivity. Electrical connection to the sample was accomplished using spring loaded gold electrodes. The luminescence emitted from the sample was monitored using a Electron Tubes bialkali PMT. The emission luminescence was filtered from the stimulation light using two 10nm FWHM bandwidth Corion 415nm interference filters.

Irradiation of the sample was done using a ^{60}Co source at 8.23 $mGys^{-1}$ or a $^{90}Sr/Y$ source at 6.79 $mGys^{-1}$. After irradiation the samples were allowed to sit for 30 minutes in order to ensure that there was no residual charge left in the 250K trap.

5.4 Data Analysis

Figure 5.9 shows a rPC using stimulation wavelengths of 514 nm (2.41 eV), 457 nm (2.71 eV), and 364 nm (3.41 eV) on samples 76, 170, and TC4. The dose given the samples was 68 Gy, the ramp rate was $3x10^{-5}$ Ws^{-1} and the maximum power was 0.3 W. Two different rPC curves are seen in the data, which will be called peak (1) for that which reaches a maximum at the shorter time and peak (2) for that which reaches a maximum at the longer time.

When stimulating at the longest wavelength (and therefore lowest energy), peak (1) reaches is maximum around 300 seconds. Peak (2) is not seen in sample 170, but the tail of peak (2) can just be seen in samples 170 and 76 for the stimulation at 514 nm. At this stimulation wavelength, the photoionization cross-section for the traps contributing to peak (1) is much higher than the photoionization cross-section for the traps contributing to peak (2). We infer that if a higher maximum stimulation power of 514 nm was used, all of peak (2) would eventually be seen. Unfortunately, this was not possible because of the power limitation of the stimulation source.

At a stimulation wavelength of 457 nm, the optical cross-sections of the various traps have changed sufficiently that both peaks (1) and (2) can apparently be fully seen. Peak (1) still has a maximum occuring at 200-300 seconds in all three samples. Peak (2) can be

seen as a bump occuring between 500-3000 seconds in samples 170 and TC4. In sample 76, peak (2) forms a very large peak reaching a maximum at ~3800s. The maximum of peak (1) has not shifted significantly because it is believed that the optical cross section for the traps responsible for peak (1) is very near the maximum, whereas, the optical cross-section from peak (2) has changed considerably, as can be seen in fig.4.5. Deconvolutions of the photoionization cross-section in chapter 4 (see fig.4.4) indicate that that there is a distributions of traps at approximately 2-2.5eV, and deeper distribution of traps around 3-3.5 eV. Thus, we assume that the traps contributing to peak (1) have a threshold optical depth of approximately 2-2.5eV and the traps contributing to peak (2) have a threshold optical depth of 3-3.5 eV. This would explain why the maximum of peak (1) changes very little, but the maximum of peak (2) shifts to a shorter time as the wavelength gets shorter. The width of peak (1) has become much more narrower in all three samples at this wavelength compared with the width of peak (1) when using 514 nm, as expected.

At a stimulation wavelength of 364 nm, the maximum of peak (2) has shifted enough that peak (1) and (2) overlap. In sample 170, this results in one broad peak, in samples 76 and TC4 it results in a distorted single peak. As the stimulation wavelength was decreased (and the stimulation energy increased), the time at which peak (2) reached a maximum decreased, yet the time that peak (1) reached a maximum remained roughly the same. This corresponds well with the simulation shown in fig.5.5.

It should be noted that after a measurement at one stimulation wavelength, the samples were annealed at 1273 K and new electrodes were applied. This is because a dose-dependent background appeared if the sample was reirradiated without annealing. This

background is most likely due to contributions from the deepest trapping states discussed in chapter 4 (3.8-5.0 eV). At 364 nm (3.41 eV), the photoionization cross-section of the deepest trapping states is not large enough to empty effectively the traps during a measurement. Thus, it appears as a dose-dependent background. The samples were annealed after each measurement to empty this charge and new electrodes were applied. Since the amount of photoconductivity measured is proportional to the area of the electrode as well as the optical absorption of the illuminated electrode, the absolute maximum currents measured at one stimulation wavelength cannot be compared with the maximum currents measured at another wavelength because the area and the thickness of the electrodes varied from deposition to deposition.

A problem with the interpretations of these measurements, however, is that the buildup of space charge in the sample, as discussed in chapter 2, distorts the shape of the peaks. Figure 5.10 shows a comparison of an rPC measurement using a constant bias and an rPC measurement using an alternating bias. The alternating bias data were obtained by taking measuring of the photocurrent at one bias for 30 seconds, averaging the data, reversing the bias, waiting 10 seconds for the sample to relax, and then measuring the photocurrent for 30 seconds with the bias reversed. It was hoped that by alternating the bias, space charge will not build up in the sample and thus the effective bias potential will remain approximately constant. As can be seen from the figure, the difference between the constant bias measurement and the alternating bias measurement is considerable. In the constant bias measurement, peak (2) reaches its maximum at ~3800 s and decays to zero by 7000-8000 s, but using an alternating bias, peak (2) has not reached its maximum by the end of the

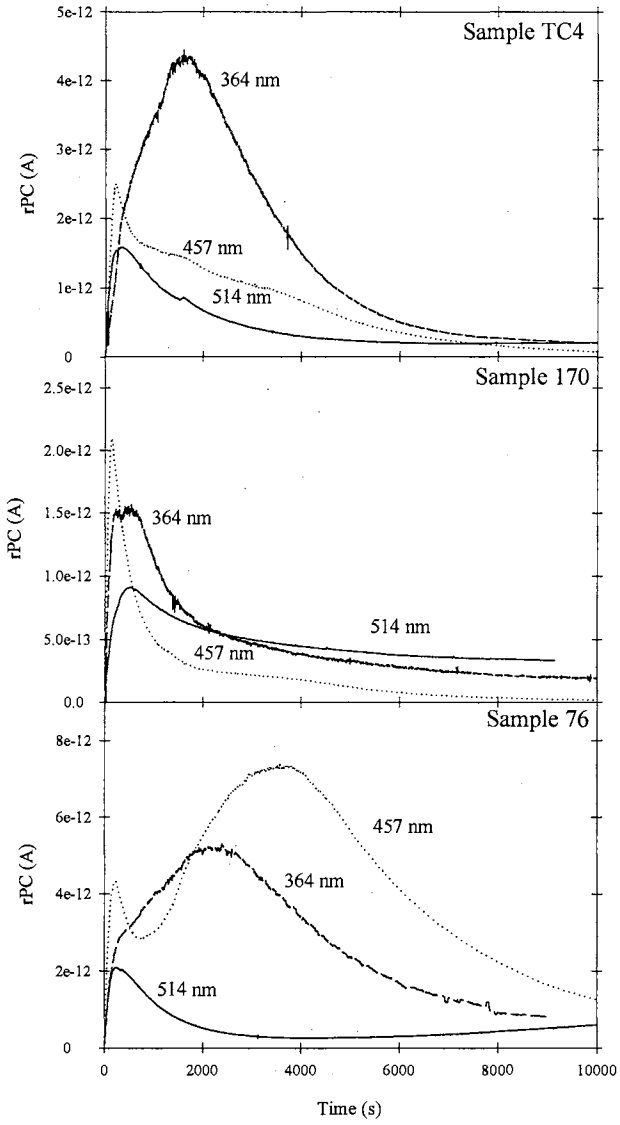

Figure 5.9 rPC measurements on 76, 170 and TC4 using stimulation light at 514 nm, 457 nm, and 364 nm. The samples were dosed with 68 Gy ^{60}Co. The ramp rate was $3x10^{-5}$ Ws^{-1}. The maximum stimulation power was 0.3 W

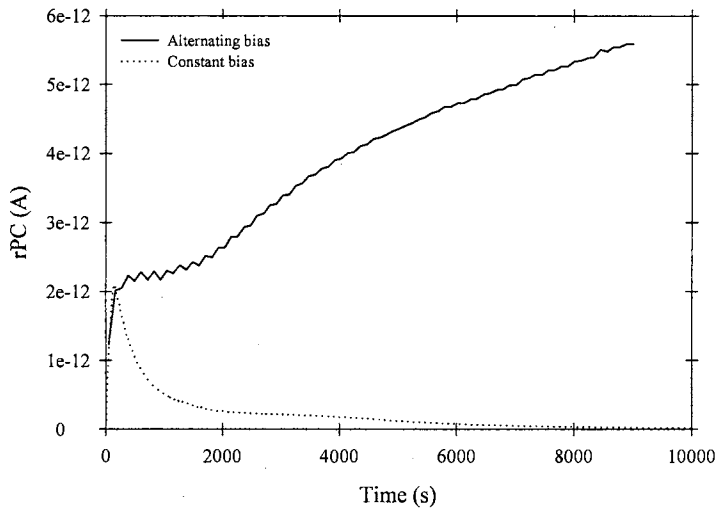

Figure 5.10 rPC taken using a constant 100 V bias (solid line) and using an alternating ± 100 V bias.

measurement (10000s). This measurement indicates that the buildup of the internal space charge in a measurement where a constant bias is applied is large enough that the applied bias is effectively cancelled by the internal space charge by ~8000s. If, directly after the measurement is finish, a higher bias is applied and the measurement retaken without reir-radiation, photoconductivity is again measured. By applying a higher bias, the internal space charge no longer cancels the applied bias, which enables photoconductivity to again be measured.

Even though the rPC measured under a constant bias is distorted, useful information can still be obtained. In order to determine which TSC trap is responsible for peak (1) and peak (2), sample 170 was pre-annealed at increasingly higher temperatures and then the rPC was taken. The sample was irradiated with 68 Gy $^{90}Sr/^{90}Y$ before each measurement

annealed at 873 K afterward to remove any remaining trapped charge. The stimulation source was the frequency doubled 532 nm line from a pulsed Nd:YAG laser with pulse with of ~100 ns and at a frequency of 4000 Hz. The ramp rate used was 5.55×10^{-5} Ws^{-1} and the maximum power was 3 W. A constant bias of 100 V was used. Figure 5.11 shows the results of that experiment. As the temperature of the pre-anneal is increased through the range of 411-500 K, the height of peak (1) decreases relative to the height of peak (2). The temperature range where the decrease in peak (1) is seen is the same range as the 450 K TSC peak. When the sample was annealed for 1 minute at 729 K, all traces of rPC peak (2) disappear. Thus, it seems to indicate that the traps responsible for the 450 K TSC peak are the same traps responsible for rPC peak (1) and the traps responsible for the 600 K TSC peak are the same traps responsible for rPC peak (2).

A comparison of fig.5.9 with the TSC of fig. 2.7, reveals that the height of peak (2) and the height of the 600K TSC peak correlate very well. The sample with the smallest 600K TSC peak (170) has the smallest peak (2) and the sample with the largest 600K TSC peak (76) also has the largest peak (2) with TC4 falling somewhere between the two. This provides additional evidence that charge responsible for rPC peak (2) is the same charge responsible for the 600 K TSC peak.

Figure 5.12 shows simultaneous rPC and rOSL taken on sample 76 using a stimulation wavelength of 514 nm at a ramp rate of 2.5×10^{-4} Ws^{-1} and a maximum power of 2.5 W. Both peaks (1) and (2) are seen in the rPC. Since the maximum stimulation power is eight times higher than in the fig.5.9, more of peak (2) is seen. In the rOSL, however, only peak (1) is seen. This indicates that even though charges from two different trapping sites

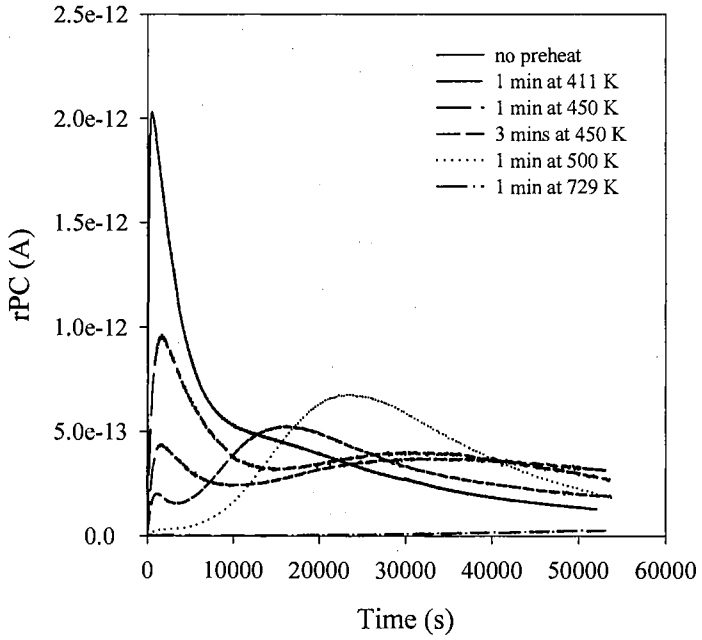

Figure 5.11 Dependence of rPC on preheat temperature. The sample was irradiated with 68 Gy $^{90}Sr/^{90}Y$ before each measurement annealed at 873 K afterward to remove any remaining trapped charge. The stimulation source was the frequency doubled 532 nm line from a pulsed Nd:YAG laser with pulse with of ~100 ns and at a frequency of 4000 Hz. The ramp rate used was 5.55×10^{-5} Ws^{-1} and the maximum power was 3 W. A constant bias of 100 V was used.

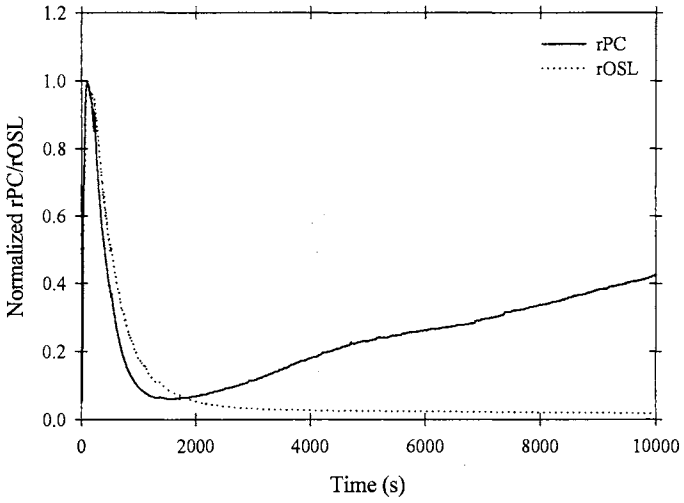

Figure 5.12 Normalized rPC and rOSL data taken simultaneously on sample 76. Both curves (1) and (2) are seen in the rPC, but only curve (1) is seen in the rOSL. The sample was irradiated with 68 Gy $^{90}Sr/^{90}Y$, the stimulation wavelength was 514 nm, the ramp rate was $2.5x10^{-4}$ Ws^{-1} and the maximum power at 10000s was 2.5 W.

are being excited into the delocalized band, only the charges associated with rPC peak (1) recombine with the F center giving rOSL peak (1). The charges associated with rPC peak (2) do not recombine with the F center. Also, note in fig.5.12 that rPC peak (1) is narrower than rOSL peak (1). This different in width is due to the space charge buildup in the rPC resulting in the rPC decaying faster than the rOSL.

As discussed earlier, the trapping centers that give rise to rPC peak (2) are thought to be the same centers that give rise to the ~573 K TSC peak. It has been a long held belief that the reason only weak F center TL was measured from these trapping centers was because of the thermal quenching phenomenon discussed in chapter 3. However, fig.5.12 indicates that the charges coming out of these traps do not recombine with the F center. This would indicate that the reason weak F center TL is measured from the 573 K trapping

center is not because the F center is quenched, but because the charge is going elsewhere. It is currently unknown where the charge released during the time that rPC peak (2) is extant actually goes.

5.5 Summery

Several conclusions can be drawn from this body of work. Multiple trapping states exist in Al_2O_3:C. Photoconductivity measurements indicate that charges in these trapping sites can be excited both optically and thermally. Deconvolutions of the photoconductivity data indicate that at least three trapping centers are excited with stimulation light in the 2.0-5.0 eV. These sites are not discrete in depth, but are distributed in energy around an average depth. Comparison of this photoconductivity with TSC indicate that these three trapping centers are likely give rise to the 450, 600 and perhaps 900 K TSC signals. Comparison of rPC and rOSL indicate not all of the charge excited optically is recombining with the F center.

5.6 Future work

Because the shapes of the rPC peaks show considerable distortions due to the space charge buildup problem, the data shown in fig.5.9 should be taken using an alternating bias in the hopes that undistorted rPC peaks could be measured.

None of the rPC data was deconvolved because of these distortions. If undistorted rPC data could be obtained, then deconvolutions of the data using the routine presented in chapter 4 will be undertaken to see how many components make up each rPC peak. If those

components can be found, then an absolute value of the photoionization cross-section can be assigned to the data in chapter 4 instead of the relative photoionization cross-section.

The rOSL emission should be measured in order to see if the charge released during rPC peak (2) recombines with another luminescence center.

More rOSL data needs be taken in order to deconvolve it and compare with the deconvolved rPC.

BIBLIOGRAPHY

1. C. Klein, C.S. Hurlbut, *Manual of Mineralogy, 20th ed.*, John Wiley and Sons, New York, USA (1985)

2. J. Yeager (ed.), M. A. Hrusch-Tupta (ed.), *Low Level Measurements*, Keithley Instruments, Inc, Cleveland, OH, USA (1998)

3. E. Dorre, H. Hubner, *Alumina*, Springer-Verlag, Berlin (1984)

4. S.W.S. McKeever, M. Moscovish, P. D. Townsend, *Thermoluminescence Dosimetry Materials: Properties and Uses,* Nuclear Technology Publishing, Ashford, UK (1995)

5. R. Boyle, *Experiments and Considerations Touching Colours*, Royal Society, 413 (1664)

6. W.H. Gitzen (ed.), *Alumina as a Ceramic Material*, The American Ceramic Society, Columbus, OH, USA (1970)

7. G.A. Rankin, H.E. Merwin, J. Am. Chem. Soc. **38**, 568 (1916)

8. F. Ulrich, Norsk. Geol. Tidsskrift **8**, 115 (1925)

9. F. Haber, Naturwiss. **13**, 1007 (1925)

10. F.C. Frary, Ind. Eng. Chem. **38**, 129 (1946)

11. K. Becker, Health Phys. **27**, 321

12. J.F. Rieke, F.J. Daniels, J. Phys. Chem. **61**, 629 (1975)

13. B.D. Evans, M. Stapelbroek, Phys. Rev. B, **18**, 7089 (1978)

14. K.H. Lee, J.H. Crawford, Phys. Rev. B. **15**, 4065 (1977)

15. B.G. Draeger, G.P. Summers, Phys. Rev. B **19**, 1172 (1979)

16. J.D. Brewer, B.T. Jeffries, G.P. Summers, Phys. Rev. B **22**, 4900 (1980)

17. B.J. Jeffries, J.D. Brewer, and G.P. Summers, Phys. Rev. B **24**, 6074 (1981)

18. G.P. Summers, in *Structures and Properties of MgO and Al_2O_3 Ceramics*, edited by W.D. Kingery, The American Ceramics Society, inc., Columbus, OH, USA (1983)

19. M.S. Akselrod, V.S. Kortov, D.J. Kravetsky, V.I. Gotlib, Radiat. Prot. Dosim **32**, 15 (1990)

20. M.S. Akselrod Private communication

21. B.G. Markey, L.E. Colyott, S.W.S. Mckeever, Radiat. Meas. **24**, 457 (1995)

22. S.W.S. McKeever, M.S. Akselrod, Radiat. Prot. Dosim. **84**, 317

23. W.H. Bragg, W.L. Bragg, *X-rays & Crystal Structure*, Bell and Sons, London (1915)

24. L. Pauling, J. Am. Chem. Soc. **51**, 1010 (1929)

25. M.S. Akselrod, N.Agersnap Larsen, V. Whitley, S.W.S. McKeever, Jour. Appl. Phys. **84**, 3364 (1998)

26. S.W.S. McKeever, *Thermoluminescence of Solids*, Cambridge University Press, Cambridge, 1985

27. S. W. S. McKeever, R. Chen, *Theory of Thermoluminescence and Related Phenomena*, World Scientific, Singapore (1997).

28. P.W. Levy, Nucl. Track Radiat. Meas. **10** (1985) 547

29. P.W. Levy, *The Encyclopedia of Physics*, R.G. Lerner and G.L. Trigg, ed., 2nd edition, VCH Publishers, inc, New York (1991) 1264

30. J.T. Randall, M.H.F. Wilkins, Proc. Roy. Soc. London **184** (1945a) 366

31. J.T. Randall, M.H.F. Wilkins, Proc. Roy. Soc. London **184** (1945b) 390

32. L. Oster, D. Weiss, N. Kristianpoller, J. Phys. D:Appl. Phys. **27**, 1732 (1994).

33. L.E. Colyott, M.S. Akselrod, S.W.S. McKeever, Radiat. Prot. Dosim. **65**, 263 (1996)

34. F.D. Walker, L.E. Colyott, N. Agersnap Larsen, S.W.S. McKeever, Radiat. Meas. 26, 711 (1996)

35. L. Bøtter-Jensen, S.W.S. McKeever, Radiat. Prot. Dosim. **65**, 274 (1996)

36. S.W.S. McKeever, M.S. Akselrod, L.E. Colyott, N. Agersnap Larsen, J. C. Polf, V. H. Whitley, Radiat. Prot. Dosim. **84**, 163 (1999)

37. E. Bulur, H. Y. Göksu, W. Wahl, Radiat. Meas. **29**, 625 (1998)

38. M.S. Akselrod, V.S. Kortov, D.J. Kravetsky, V.I. Gotlib, Radiat. Prot. Dosim. **32**, 15 (1990)

39. M.S. Akselrod, V.S. Kortov, D.J. Kravetsky, E.A. Goreleva, Radiat. Prot. Dosim. **47**, 159 (1993)

40. G. Kitis, S. Papadopoulos, S. Charalambous, J. Tuyn, Radiat. Prot. Dosim. **55**, 183 (1994)

41. V.S. Kortov, I.I. Milman, V.I. Kirpa, J. Lesz, Radiat. Prot. Dosim, **55**, 279 (1994)

42. T.I. Gimadova, T.S. bessanova, I.A. Tale, A. Avvakumova, S.V. Boadyachevsy, Radiat. Prot. Dosim. **33**, 47 (1990)

43. V.S. Kortov, I.I. Milman, Radiat. Prot. Dosim. **65**,179 (1996)

44. I.I. Milman, V.S. Kortov, V.I. Kirpa, Phys. Solid State **37**, 625 (1995)

45. M.S. Akselrod, V.I. Kirpa, Proceedings of the All-Union Symposium on Luminescence Detectors and Transformers of Ionizing Radiation, Lviv, 30 (1989) [in Russian]

46. L.A. Avvakumova, T.S. Bessonova, S.V. Bodyachevskii, T.I. Gimadova, I.B. Keirim-Markus, Abstract of paper presented at the Sixth All-Union Conf. On Radiation and Chemistry of Ionic Crystals, Riva, Part 2, 335 (1986) [in Russian]

47. I.I. Milman, V.S. Kortov, S.V. Nikiforov, Radiat. Meas. **29**, 401 (1998)

48. P. Kulis, V. Springis, I. Tale, Abstract of paper presented at the LUMDETR 97 Conference, Ustron, Poland, October (1997)

49. S.W.S. Mckeever, L. Bøtter-Jensen, N. Agersnap Larsen, G.A.T. Duller, Radiat. Meas. **27**, 161 (1997)

50. J. D. Brewer, B. T. Jeffries, G. P. Summers, Phys. Rev. B**22**, 4900 (1980)

51. G. P. Summers, Radiat. Prot. Dosim. **8**, 69 (1984)

52. N. Agersnap Larsen, L. Bøtter-Jensen and S.W.S. McKeever, Radiat. Prot. Dosim. **84**, 87, (1999)

53. H.G. Grimmeiss, L-Å. Ledebo, J. Phys. C, **8**, 2615 (1975)

54. H.G. Grimmeiss, L-Å. Ledebo, J. Appl. Phys. **46**, 2155 (1974)

55. N.Agersnap Larsen, S.W.S. McKeever, (in preparation)

56. M.S. Akselrod and S.W.S. McKeever, Radiat. Prot. Dosim. **81**, 167 (1999)

57. M.S. Akselrod, V.S. Kortov, Radiat. Prot. Dosim., **33**, 123 (1990)

58. M.G. Springis, J.A. Valbis, Phys. Stat. Sol. (b) **123**, 335, (1984)

59. Yong-Nian Xu, W.Y. Ching, Phys. Rev. B, **43**, 4461 (1991)

60. M.S. Akselrod and E.A. Goreleva, Radiat. Meas. **21**, 143 (1993)

61. E. Bulur, Radiat. Meas. **26**, 701 (1996)

VITA

Von Howard Whitley

Candidate for the Degree of

Doctor of Philosophy

Thesis: OPTICAL AND THERMAL STUDIES OF DEEP LEVELS IN ANION DEFICIENT AL_2O_3:C

Major Field: Physics

Biographical:

Personal Data: Born in Granbury, Texas, on November 26, 1971, the son of Deborah Strickland and Jimmy Whitley.

Education: Received Bachelor of Science degree in Physics from the University of Texas, Austin, Texas, in May 1994. Completed the requirements for the Doctor of Philosophy degree in Physics at Oklahoma State University in May, 2000.

Profession Experience: Teaching assistant from August 1994 to May 1996; Research assistant from May 1996 to May 2000. Post-doc at Scottish Universities Research & Reactor Centre, East Kilbride, Scotland, May 2000.